

Taming electronic decoherence in one-dimensional chiral ballistic quantum conductorsC. Cabart,¹ B. Roussel,^{1,2} G. Fève,³ and P. Degiovanni^{1,*}¹*Univ Lyon, Ens de Lyon, Université Claude Bernard Lyon 1, CNRS, Laboratoire de Physique, F-69342 Lyon, France*²*European Space Agency - Advanced Concepts Team, ESTEC, Keplerlaan 1, 2201 AZ Noordwijk, The Netherlands*³*Laboratoire Pierre Aigrain, Ecole Normale Supérieure-PSL Research University, CNRS, Sorbonne Université, Université Paris Diderot-Sorbonne Paris Cité, 24 rue Lhomond, 75231 Paris Cedex 05, France*

(Received 12 April 2018; revised manuscript received 3 August 2018; published 5 October 2018)

Although interesting per se, decoherence and relaxation of single-electron excitations induced by strong effective screened Coulomb interactions in Quantum Hall edge channels are an important challenge for the applications of electron quantum optics in quantum information and quantum sensing. In this paper, we study intrinsic single-electron decoherence within an ideal single-electron channel with long-range effective Coulomb interactions to determine the influence of the material and sample properties. We find that weak-coupling materials characterized by a high velocity of hot-electron excitations may offer interesting perspectives for limiting intrinsic decoherence due to electron/electron interactions. We discuss quantitatively how extrinsic decoherence due to the coupling with the channel's electromagnetic environment can be efficiently inhibited in specifically designed samples at $\nu = 2$ with one closed edge channel and we propose a realistic geometry for testing decoherence control in a Hong-Ou-Mandel experiment.

DOI: [10.1103/PhysRevB.98.155302](https://doi.org/10.1103/PhysRevB.98.155302)**I. INTRODUCTION**

Over the last decade, a considerable effort has been devoted to the development of quantum coherent nanoelectronics with the aim of controlling electronic quantum transport down to the single-particle level [1,2]. This has led to the emergence of electron quantum optics [3–5], which aims at manipulating electrons in a ballistic quantum conductor just as photons in quantum optics setups. This perspective had initially risen strong hopes for on-chip quantum information processing using single electrons as quantum information carriers [6–8].

However, electron quantum optics differs from quantum optics because electrons experience electronic decoherence and relaxation induced by effective screened Coulomb interactions. The weakness of these effects close to the Fermi surface in normal 3D metals justifies building the Landau-Fermi liquid theory [9] on the notion of electronic quasiparticles [10]. By contrast, Coulomb interaction is expected to completely destroy electronic quasiparticles in 1D systems thus giving rise to the Luttinger liquid paradigm [11], which is experimentally relevant for quantum wires [12,13].

More recently, the electronic quasiparticle destruction has been evidenced in the $\nu = 2$ quantum Hall edge channel system by nonequilibrium distribution relaxation studies [14], before being confirmed at the single-particle level by Hong-Ou-Mandel (HOM) interferometry experiments [15,16]. Recent Mach-Zehnder interferometry (MZI) experiments [17] have also shown the strong effect of Coulomb interactions although the most commonly used model based on effective screened short-range interactions [18] fails to reproduce the observed saturation of electronic decoherence [19]. These recent results suggest that our understanding of quantitative

models of electronic decoherence in quantum Hall edge channels still needs to be sharpened.

Moreover, using single-electron excitation as carriers of quantum information requires a high degree of control from their generation to their detection, and during their propagation. Several single-electron sources have been developed over the years, from the mesoscopic capacitor [20] to single-electron pumps [21,22] and more recently the Leviton source [23]. Other systems aim at injecting electrons at very high energies [24] using dynamically driven dots or at transporting them using surface acoustic waves [25]. The maturation of technology may lead to the development of controlled sources able to emit specifically tailored electronic wave packets [26–28].

On the detection side, a full quantum current analyzer has been developed to extract the single-electron wave functions present within a time-periodic electric current [29,30]. Dynamical quantum dots are also envisioned to probe single-electron coherence in a time-dependent and energy-selective way [22,31].

But controlling the dynamics of propagating single to few electron excitations is still a challenge, even though it is crucial for the applications of electron quantum optics to quantum information processing or to quantum metrology of charge and electrical currents. For all these reasons, it is thus time to ask to what extent electronic decoherence can be tamed in experimentally relevant systems. In this paper, we address this question within our recently developed nonperturbative framework for studying single-electron decoherence in a chiral 1D conductor [32,33].

First of all, we show that the effective fine structure constant within the material, which depends on its intrinsic properties as well as its fabrication through gating, strongly influence electronic decoherence. In particular, by discussing

*Pascal.Degiovanni@ens-lyon.fr

electronic decoherence within ideal $\nu = 1$ edge channels, we suggest that materials such as exfoliated graphene and AlGaAs/GaAs respectively correspond to weak and strong coupling materials, the former being more favorable for preserving electronic decoherence than the latter.

Next, by performing an in-depth discussion of various geometries which have been used in recent experiments [34,35], we suggest that an efficient control of single-electron decoherence could be achieved within edge channels of an AlGaAs/GaAs 2D electron gas in the integer quantum Hall regime at $\nu = 2$. A new sample design is proposed for testing our predictions in a HOM interferometer.

Finally, our work also points out to the possibility of discriminating among various models of effective screened electronic Coulomb interactions using HOM interferometry experiments. We also show that samples based on passive decoherence control offer interesting perspectives for single edge-magnetoplasmon generation, thus connecting electron quantum optics to quantum plasmonics and microwave quantum optics.

This paper is structured as follows. In Sec. II, we briefly review the basic concepts of electron quantum optics and the physics of single-electron decoherence in quantum Hall edge channels. Then, analytical models of screened Coulomb interactions for the physical situations relevant for the present paper will be introduced and the corresponding edge-magnetoplasmon scattering will be discussed. Section III is devoted to electronic decoherence. Decoherence at filling fraction $\nu = 1$ in the dissipationless case will enable us to discuss the influence of the sample's material. We will also discuss to what extent an HOM experiment could help discriminate between short and long-range effective interactions in the $\nu = 2$ system. Finally, Sec. IV is devoted to decoherence control for single-electron excitations by sample design.

II. ELECTRON QUANTUM OPTICS AND FINITE-FREQUENCY QUANTUM TRANSPORT

A. Electron quantum optics

1. Electronic coherence

The key concepts of electron quantum optics are electronic coherences defined by analogy with photon coherences introduced by Glauber for photons [36]. The first-order electronic coherence at position x [37–39] $\mathcal{G}_{\rho,x}^{(e)}(t|t') = \text{Tr}(\psi^\dagger(x,t)\rho\psi(x,t'))$, where ψ is the electronic annihilation operator, contains all information on the single-electron wave functions that can be extracted from the system at position x . To simplify notation, because our detection setup is at a fixed position x , we will drop it from all equations in the following. Electronic coherence is most conveniently visualized using a real valued time/frequency representation called the electronic Wigner function, defined as [40]

$$\mathcal{W}_\rho^{(e)}(t, \omega) = \int v_F \mathcal{G}_\rho^{(e)}\left(t + \frac{\tau}{2}, t - \frac{\tau}{2}\right) e^{i\omega\tau} d\tau \quad (1)$$

The electronic Wigner function is directly related to physically relevant quantities: first of all, integrating over ω leads to the average time-dependent current and time averaging gives the electronic distribution function.

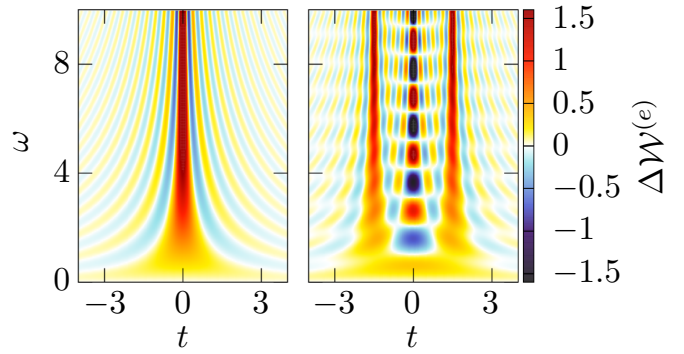


FIG. 1. (Left) Excess electronic Wigner function for a single electronic state of the form $\psi^\dagger(t=0)|F\rangle$ measured at $x=0$. (Right) Excess electronic Wigner function for a quantum superposition $(\psi^\dagger(-\tau/2) + \psi^\dagger(\tau/2))|F\rangle/\sqrt{2}$ ($\tau=3$ on this specific example). The interference contribution is clearly visible and overlaps with each localized excitation contribution for $\omega\tau \lesssim 1$.

More generally, the electronic Wigner function contains all the information on the single-particle states contained in the system. These in particular include the reference state which is the Fermi sea at zero temperature or the equilibrium state at non zero temperature. In full generality, the excess electronic Wigner function is defined by

$$\mathcal{W}_\rho^{(e)}(t, \omega) = f_{\mu, T_{\text{el}}}(\omega) + \Delta\mathcal{W}_\rho^{(e)}(t, \omega) \quad (2)$$

where $f_{\mu, T_{\text{el}}}(\omega)$ is the Fermi-Dirac distribution function for chemical potential μ and electronic temperature T_{el} which is the electronic Wigner function at equilibrium corresponding to the situation where all the sources are switched off.

Let us now briefly review the electronic Wigner function associated with single-electron excitations on top of the Fermi sea, that is at zero temperature. Generically, a single-electron excitation with a normalized wave packet φ_e above the Fermi sea,

$$|\varphi_e, F\rangle = \int_{-\infty}^{+\infty} \varphi_e(t)\psi^\dagger(t)|F\rangle dt, \quad (3)$$

is a quantum superposition of excitations obtained by adding a perfectly localized electronic excitation on top of the Fermi sea. To understand how the excess electronic Wigner function of the state $|\varphi_e, F\rangle$ looks like in physically relevant examples, let us start by considering the electronic Wigner function for a perfectly localized excitation $\psi^\dagger(0)|F\rangle$. It is, up to normalization, depicted on the left panel of Fig. 1. As expected from the Heisenberg uncertainty principle, such an excitation is not limited in energy and, when injected at energy $\varepsilon > 0$ above the Fermi level, the Wigner function tends to spread over a time scale \hbar/ε . Before discussing the general case, let us consider the Wigner function of a quantum superposition of two such excitations created at times $t_1 = \tau/2$ and $t_2 = -\tau/2$. It contains a contribution for each of the excitations within the superposition and an interference contribution located at time $t \simeq (t_1 + t_2)/2 = 0$ as depicted on the right panel of Fig. 1.

When considering an arbitrary electronic wave packet φ_e , these interference contributions are responsible for cancellations which, in the case of the Landau excitation emitted at energy $\hbar\omega_0$ above the Fermi level, localize the main contribution

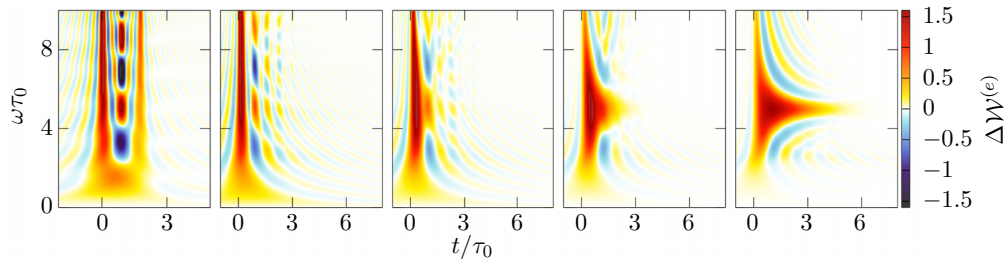


FIG. 2. Numerical reconstruction of the excess Wigner function for a Landau excitation with emission energy $\hbar\omega_0$ and duration τ_0 with $\omega_0\tau_0 = 5$. Each panel depicts the Wigner function associated with a finite sum $\sum_{j=1}^N \varphi_e(t_j)\psi^\dagger(t_j)|F\rangle$, where the times t_j are sampled randomly using the probability distribution $|\varphi_e(t)|^2$. From left to right, panels show the results corresponding to $N = 2, 10, 25, 100$, and $N = 500$.

to the excess electronic Wigner function close to the injection energy ω_0 . The Landau wave packet, given by [37,40]

$$\tilde{\varphi}_e(\omega) = \frac{\mathcal{N}_0\Theta(\omega)}{\omega - \omega_0 - i/2\tau_0}, \quad (4)$$

where τ_0 denotes the excitation lifetime, will indeed be used as our main example through this whole text because of its experimental relevance for the mesoscopic capacitor in the ideal single-electron source regime [20,41,42].

The emergence of the electronic Wigner function of a Landau excitation through destructive interferences is depicted on Fig. 2: the full excess electronic Wigner function is reconstructed from the excess Wigner function of a quantum superposition of more and more localized electronic excitations at times t_j , each of them weighted by the value of the electronic wave function $\varphi_e(t_j)$. Each panel is obtained by choosing randomly the times t_j according to the probability density for the wave packet φ_e and then computing the excess single-electron coherence associated with the quantum superposition $\sum_{j=1}^N \varphi_e(t_j)\psi^\dagger(t_j)|F\rangle$. Increasing N shows, on this example, how the specific form of the excess Wigner function arises from quantum interferences between its different time-localized contributions.

The other important example is the recently observed [23] Leviton excitation introduced by Levitov, Lee, and Lesovik [43] and whose wave packet is given by

$$\varphi_e(t) = \sqrt{\frac{\tau_0}{2\pi}} \frac{1}{t + i\tau_0}. \quad (5)$$

This excitation is quite special as it is the only mono-electronic excitation that can be created by applying a carefully designed classical voltage drive to an ohmic contact [44]. The excess Wigner functions for both types of single-electronic excitations used in this paper are depicted on Fig. 3.

2. Hong-Ou-Mandel interferometry

Various methods have been proposed to access single-electron coherence. First of all, measurement of the electronic distribution function via energy filtering [45] or of the average electrical current in the time or frequency domain only recovers a partial information on single-electron coherence [40]. As in optics, single-particle interferometry in an ideal Mach-Zehnder interferometer could give access to single-electron coherence by unbalancing the interferometer [38,39] but, unfortunately, Coulomb interactions prevent such a tomographic

reconstruction. Electronic dephasing limits single-particle interferometry just as atmospheric turbulence limited astronomy in the optical domain during most of the 20th century. Exactly as in astronomy, a solution to circumvent difficulties related to dephasing within the interferometers is then to go to the electronic counterpart of intensity interferometry, that is to perform two-particle interference [46] as in Hong-Ou-Mandel and Hanbury Brown and Twiss interferometry. These intensity interferometry techniques have now spread widely beyond the field of optics [47,48].

In our framework, the low-frequency Hong-Ou-Mandel (HOM) noise signal for two electronic sources is directly proportional to the overlap of the excess Wigner functions of the two sources [40], a fact directly exploited in electronic tomography protocols [29,37,49] and recent studies of electronic decoherence [15,16].

More precisely, the outgoing low frequency excess current noise in an HOM experiment is the sum of three contributions,

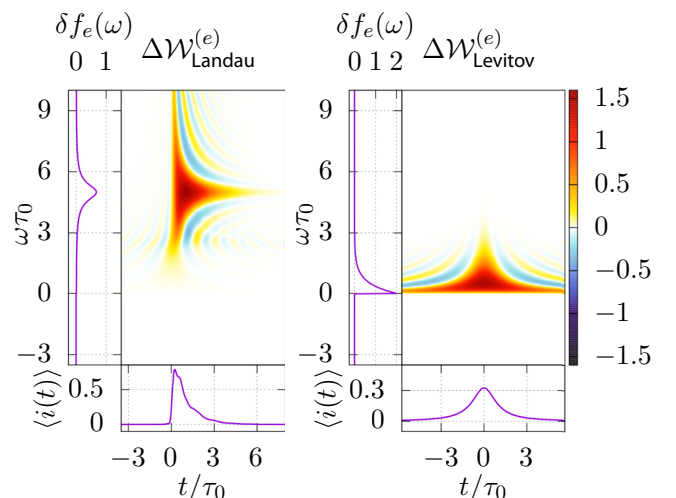


FIG. 3. Density plot of the Wigner function of a Landau excitation with parameters $\omega_0\tau_0 = 5$, left, and an $n = 1$ Leviton excitation, right, as a function of t/τ_0 and $\omega\tau_0$. Marginals are also plotted, giving access to the average current as a function of time (bottom of each plot) and the excess occupation number as a function of energy (left of each plot). These two excitations are single-electronic and are respectively energy- and time-resolved, with a Lorentzian profile. In the case of the Landau excitation, we obtain the form given by the superposition depicted on the right panel of Fig. 2.

the two first ones involving the excess current noise $\Delta\mathcal{S}_{1\text{in}}$ and $\Delta\mathcal{S}_{2\text{in}}$ in the incoming channels and the third one \mathcal{Q} that contains two-particle interference effects [5,37]:

$$\Delta\mathcal{S}_{1\text{out}} = \mathcal{R}^2\Delta\mathcal{S}_{1\text{in}} + \mathcal{T}^2\Delta\mathcal{S}_{2\text{in}} + \mathcal{R}\mathcal{T}\mathcal{Q} \quad (6)$$

in which \mathcal{T} and $\mathcal{R} = 1 - \mathcal{T}$ denote the transmission and reflection probabilities across the electronic beam splitter. When the two sources are switched on, the two-particle interference contribution is the sum of three contributions [29,40]: the first two ones are the partition excess noise obtained when only one of the two sources is switched on and the other one off. They arise from two-particle interferences between excitations emitted by the on source and the ones present within the Fermi sea. At zero temperature, it corresponds to the total number of excitations (holes and electrons) emitted by each of the source separately [50]. The last contribution comes from two-particle interferences between the excitations that are emitted when both sources are on. It is given by [40]

$$\mathcal{Q}_{\text{HOM}} = -2e^2 \int_{\mathbb{R}} \overline{\Delta\mathcal{W}_1^{(e)}(t, \omega) \Delta\mathcal{W}_2^{(e)}(t, \omega)} \frac{d\omega}{2\pi}, \quad (7)$$

where $\Delta\mathcal{W}_a^{(e)}(t, \omega)$ denotes the incoming excess electronic Wigner function in channel $a = 1, 2$ and $\overline{X(t)}$ denotes the time average of $X(t)$.

When considering classical voltage pulses or an ideal single-electron source, or an ac source, the source's excess current noise vanishes in the limit of low frequencies. In this case, measuring the excess current noises when the two electronic sources are, respectively, (on,off), (off,on), and (on,on) directly gives access to [5]

$$\Delta q = \frac{\mathcal{Q}_{\text{on,on}}}{\mathcal{Q}_{\text{on,off}} + \mathcal{Q}_{\text{off,on}}}, \quad (8)$$

which is called the HOM signal. The HOM curve is then obtained by varying the time delay between the two electronic sources. In quantum signal processing terms, the HOM interferometer encodes the overlap of two quantum signals (the excess single-electron coherence) emitted by each source into a measurable quantity (the low-frequency excess current noise). It performs an on-chip overlapping analysis of quantum signals [4].

In the case of two identical sources, the HOM curve is a measure of the time-delayed self overlap of the source's excess Wigner function and as such, contains information on single-particle states that are emitted. For instance, in the absence of electronic decoherence, two identical sources emitting exactly one single-electron excitation per period lead to $\Delta q = 0$ when they are synchronized whereas $\Delta q \rightarrow 1$ asymptotically when the two sources are maximally desynchronized. More generally, a dip in the HOM curve is observed close to perfect synchronization and its depth is a measure of the indistinguishability between the excitations emitted by both sources [5]. As we shall discuss more explicitly in the next section, by imprinting information on the single-electron excitation in an external environment or by transferring them into higher order correlations, interactions lead to electronic decoherence and thus decrease the HOM dip.

B. The physics of single-electron decoherence

In the original discussion of the decay of an electronic quasiparticle by Landau [10], electronic decoherence arises from electron/hole pair creation by the time and space dependent electric potential generated by the bare charge injected at a given energy above the Fermi sea. In this situation, the single-particle excitation experiences decoherence whereas the whole electronic fluid remains coherent. More than 50 years later, the discovery of dynamical Coulomb blockade [51,52] showed us that electronic relaxation could also arise from the emission of photons into the electromagnetic environment of the conductor. Our present understanding of single-electron decoherence in quantum Hall edge channels [32,33] appears as a combination of these two effects.

When the edge channel under consideration is coupled to environmental degrees of freedom that can take energy away, this coupling leads to entanglement between the electronic fluid and its external environment. Consequently, the edge channel experiences a many-body decoherence. For example, this happens at $\nu = 2$: interchannel Coulomb interactions generically induce entanglement between the two edge channels. This is responsible for the fast relaxation of Landau electronic excitations compared to the Levitov excitations [33]. This striking difference between these two excitations can be traced back to the fact that Levitov excitations, being edge-magnetoplasmon coherent states, are pointer states [53] with respect to Coulomb interaction. By contrast, other single-electron excitations are quantum superpositions of edge-magnetoplasmon coherent states, so that many-body decoherence kills interferences between these coherent components. This leads, for example, to a suppression of the interferences which are responsible for localization of the Wigner function of a Landau excitation around its emission energy (see Fig. 2). As demonstrated by experimental decoherence studies at $\nu = 2$ through HOM interferometry [15] as well as by Mach-Zehnder interferometry [17], this is, so far, the dominant cause of electronic decoherence in these experiments.

The second cause for single-electron decoherence is the generation of electron/hole pairs in the same channel induced by voltage fluctuations within the interacting region. This is the only source of electronic decoherence when the edge channel is not coupled to environmental channels. This purely intrinsic process can be interpreted as the spreading of the quantum information associated with the injected single electron towards higher-order coherences. Because of the Pauli principle induced phase space limitations, we expect it to be less stringent than excitation emission into the external environment. The decoherence scenario is thus expected to be significantly different and more favorable to decoherence control than when the edge channel is capacitively coupled to other conductors.

Inspired by this idea, we will therefore study electronic decoherence within an ideal $\nu = 1$ quantum Hall edge channel. It is solely influenced by the intrinsic properties of the edge channel, that is the intrinsic and substrate material properties as well as its gating, thus giving us new insight on the role of the material in electronic decoherence.

Cutting off the possibility to generate excitations within the electromagnetic environment is also the basic idea behind passive decoherence protection by sample design at $\nu = 2$. The samples studied in Refs. [34,35] are based on blocking

electronic relaxation and decoherence within one of the two edge channels by closing the other one on itself.

As known from previous studies [32,33], quantitatively studying the electronic decoherence scenarios in these different situations requires an understanding of the effect of effective screened Coulomb interactions on the electronic fluid. As we shall recall now, in the linear response regime, it is completely encoded into the finite-frequency admittance matrix of the system.

C. Interactions and edge-magnetoplasmon scattering

1. General method

During their propagation, electronic excitations experience screened Coulomb interactions within the conductor and with charges located in nearby conductors. However, in a regime of linear response for all conductors involved, interaction effects can be described within the edge-magnetoplasmon scattering formalism, which describes how the bosonic edge-magnetoplasmon modes are altered within the interaction region. The key point is that, in one dimension, the bosonization framework enables describing fermions with a linear dispersion relation in terms of chiral bosons [54,55], which, in the integer QHE are the edge magnetoplasmon modes [56]. It is thus very well suited to describe electron quantum optics experiments since the energy scale of the excitations generated by single-electron sources which is the order of a few tens of μeV is one to two order of magnitudes smaller than the energy scale at which nonlinearities in the dispersion relation strongly manifest themselves, such as the cyclotron energy at a few tesla (typically a few meV in AlGaAs/GaAs).

Typical electron quantum optics excitations involve propagation between a source and a detector (usually a QPC) that delimitate a length l region of a quantum Hall edge channel. Within this region, electrons experience intrachannel Coulomb interactions as well as Coulomb interactions with other edge channels [see Fig. 4(a)] or with an external gate connected to an impedance [see Fig. 4(b)]. For the edge channel under consideration, electronic degrees of freedom are described by the bosonic field $\phi(x, t)$ defined from the excess charge density by

$$:(\psi^\dagger\psi): (x, t) = \frac{1}{\sqrt{\pi}} (\partial_x\phi)(x, t), \quad (9)$$

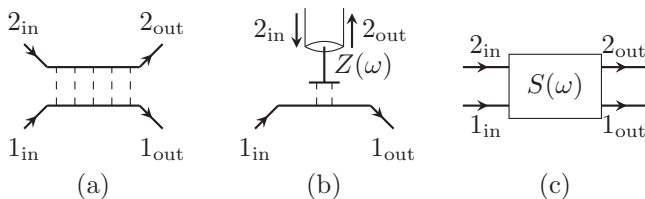


FIG. 4. The edge-magnetoplasmon scattering approach describes many situations, such as, for example, (a) two copropagating edge channels capacitively coupled over a distance l , (b) a chiral edge channel capacitively coupled to a linear external circuit described by a frequency dependent impedance $Z(\omega)$. (c) Solving the equation of motions leads to a frequency dependent scattering matrix $S(\omega)$ between the channel's edge-magnetoplasmon modes and the bosonic modes of the other system.

where $:(\psi^\dagger\psi):$ denotes the fermionic normal ordering with respect to the reference Fermi level. Its equation of motion is given by

$$(\partial_t + v_F\partial_x)\phi(x, t) = \frac{e\sqrt{\pi}}{h} U(x, t), \quad (10)$$

where $U(x, t)$ denotes the potential along the edge channel. Assuming we are in a linear screening regime within the edge channel as well as for the external elements capacitively coupled to it, the potential $U(x, t)$ is linear in terms of both the bosonic fields associated with the other edge channels and the bosonic dynamical variables describing other circuit elements. In the case of a gate coupled to an external circuit, these would be the bosonic modes associated with the transmission line representation of the circuit's impedance. In the same way, the edge-magnetoplasmon modes of the current channel appear within source terms for the linear equations describing bosonic modes for the other edge channels and circuit elements.

The interaction region being of finite length, solving the equations of motion leads to an expression for the outgoing fields in terms of the incoming fields. Note that because the problem is time translation invariant, the solution can be expressed in terms of an elastic scattering matrix $S(\omega)$ linking the incoming and outgoing bosonic modes [see Fig. 4(c)]. With our definition of bosonic modes, energy conservation implies that the scattering matrix is unitary.

The edge-magnetoplasmon scattering matrix is directly related to the dimensionless finite-frequency admittance $g_{\alpha,\beta}(\omega) = R_K G_{\alpha,\beta}(\omega)$ ($R_K = h/e^2$ being the quantum of resistance) defined as the ratio of the derivative of total current coming into the sample through the edge channel α with respect to the voltage applied to the reservoir feeding the edge channel β . Such a relation had been derived in the case of quantum wires [57–59], which are nonchiral Luttinger liquids. In the present case of chiral quantum Hall edge channel at integer filling fractions, it takes the following form [60]:

$$g_{\alpha\beta}(\omega) = \delta_{\alpha,\beta} - S_{\alpha\beta}(\omega). \quad (11)$$

In particular, we shall denote $g(\omega) = 1 - S_{11}(\omega)$ the finite frequency admittance of edge channel 1 in geometries depicted on Fig. 4.

Relating the edge-magnetoplasmon transmission amplitude $t(\omega) = S_{11}(\omega)$ to $g(\omega)$ also constrains it. The finite frequency admittance $g(\omega)$ is the physical response function of a passive electric dipole and, as such, admits an analytic continuation to negative frequencies satisfying $g(\omega)^* = g(-\omega)$ thus implying the same property for $t(\omega) = 1 - g(\omega)$. Being the response of a passive circuit, $g(\omega)$ obeys the positive reality condition first proposed by Cauer [61] and then proven by Brune [62]. With our convention, this means that for $z = \sigma + i\omega$, $z \mapsto g(z)$ is analytic in the half plane $\Re(z) < 0$ and

$$\Re(g(z)) > 0 \quad \text{when} \quad \sigma < 0, \quad (12a)$$

$$\Im(g(z)) = 0 \quad \text{when} \quad z \in \mathbb{R}^-. \quad (12b)$$

The analyticity condition ensures causality of the current response. The two other conditions express that, when driven by a time-dependent voltage, the electric dipole dissipates energy and does not produce it. As we shall see, these conditions constrain the effective Coulomb interaction models that can be used.

Finally, since the edge-magnetoplasmon scattering matrix depends on the precise form of the electric potential within the wire $U(x, t)$, analytical models are often approximative descriptions of the real physics of the sample in which electrostatics plays an important role [63–65]. A more quantitative description would rely on a microscopic modeling of the system using first-principles modeling and taking into account interactions through, for example, a self-consistent Hartree treatment of the problem as in Ref. [66]. However, Eq. (11) shows that edge-magnetoplasmon scattering amplitudes can also be accessed using finite-frequency admittance measurements. This has indeed been done in the case of the $\nu = 2$ quantum Hall edge channel system [67]. Here, we will consider an ideal $\nu = 1$ edge channel with finite range intrachannel interactions as well as specific geometries of two interacting edge channels ($\nu = 2$) in which one of the edge channels is closed. Let us now discuss edge-magnetoplasmon scattering models relevant for these cases.

2. The $\nu = 1$ case

For a single edge channel with Coulomb intrachannel interactions, the edge-magnetoplasmon scattering matrix reduces to a frequency dependent transmission coefficient $t(\omega)$, which, in the absence of dissipation, satisfies $|t(\omega)| = 1$.

Short-range effective screened Coulomb interactions correspond to a renormalization of the edge-magnetoplasmon velocity and therefore to a linear dependence of the phase of $t(\omega)$ in ω , $t(\omega) = e^{i\omega\tau(l)}$, where $\tau(l)$ is the renormalized time of flight. By contrast, finite range interactions lead to a nonlinear frequency dependence of the phase of $t(\omega)$. We shall write $t(\omega) = e^{i\omega\tau(l,\omega)}$ where the time of flight now depends on ω through a frequency dependent velocity for the edge magnetoplasmons, $\tau(l, \omega) = l/v(\omega)$. Since $t(\omega)^* = t(-\omega)$, $v(\omega)$ can be extended analytically to negative frequencies by $v(-\omega) = v(\omega)$.

A simple model of a $\nu = 1$ edge channel with an interaction region of length l , capacitance C and bare Fermi velocity v_F is presented in Appendix B. This model depends on the dimensionless ratio $\alpha = (e^2/C)/(\hbar v_F/l)$ of the Coulomb energy for the interaction region to the associated kinetic energy. Let us note that C being the capacitance of the interaction region that is roughly similar to a 1D wire, for large enough l to neglect boundary effects, $C \simeq 2\pi\epsilon_0\epsilon_r l$ up to a geometrical factor. Consequently, α does not depend on l but behaves as [68]

$$\alpha \simeq \frac{\alpha_{\text{qed}}}{\pi\epsilon_r} \times \frac{c}{v_F} \times (\text{geometrical factor}), \quad (13)$$

where α_{qed} denotes the fine-structure constant, ϵ_r the relative permittivity of the material, and v_F the bare Fermi velocity. Consequently, α can be interpreted as the renormalized dimensionless effective fine structure constant within the material.

As expected, the edge-magnetoplasmon transmission amplitude $t(\omega) = e^{i\omega l/v(\omega)}$ exhibits a nonlinear dependence of the phase:

$$t(\omega) = e^{i\omega l/v_F} \frac{1 + A(\omega, l)e^{-i\omega l/(2v_F)}}{1 + A(\omega, l)e^{i\omega l/(2v_F)}}, \quad (14)$$

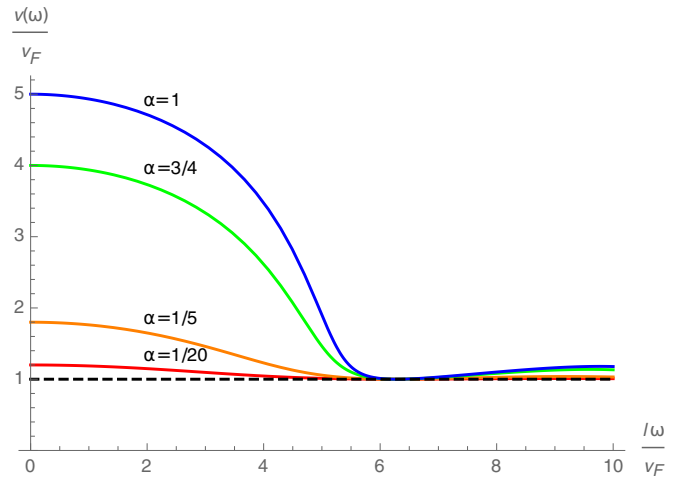


FIG. 5. Velocity $v(\omega)/v_F$ corresponding to $\exp(i\omega l/v(\omega))$ given by Eq. (14) in terms of $\omega l/v_F$ for $\alpha = 1/20$ (graphene), $\alpha = 1/5$, $\alpha = 3/4$ (AlGaAs/GaAs), and $\alpha = 1$.

where

$$A(\omega, l) = 4\alpha \operatorname{sinc}\left(\frac{\omega l}{2v_F}\right). \quad (15)$$

The edge-magnetoplasmon velocity $v(\omega)$ decreases from $v_0 = (1 + 4\alpha)v_F$ to its asymptotic value $v_\infty = v_F$ showing some mild oscillations (see Fig. 5) arising from the sharp position dependence of the interaction potential at the boundary of the interaction region.

Realistic estimates for the coupling constant α are detailed in Appendix B. In AlGaAs/GaAs, $\alpha \simeq 0.75$ for $v_F \simeq 10^5$ m/s thus leading to a ratio $v_0/v_F = 4$. By comparison, a similar estimate for exfoliated graphene on a silicon oxide surface [69] leads to $\alpha \simeq 0.05$ assuming $v_F \simeq 10^6$ m/s, and thus to $v_0/v_F \simeq 1.2$. Provided it has such a high Fermi velocity, this form of graphene may thus correspond to a weak coupling whereas AlGaAs/GaAs leads to strong coupling. A small coupling constant has drastic consequences on electronic decoherence as will be discussed in Sec. III C. Therefore studying single-electron decoherence in the edge channels of graphene at $\nu = 1$ may be a way to test whether or not it is a weak or a strong coupling material.

We expect a more realistic model of intrachannel interactions to lead to a qualitatively similar but smoother behavior of $v(\omega)$. Key features are the two different asymptotic velocities v_0 and v_∞ in the limits $\omega \rightarrow 0$ and $\omega \rightarrow +\infty$. The infrared velocity v_0 is the velocity of low energy edge-magnetoplasmon modes and should therefore be called the plasmon velocity. Due to Coulomb interactions, it is expected to be higher than the velocity of high-energy excitations which do not experience interactions for a long time. Reasonable phenomenological models for $v(\omega)$ should thus interpolate between v_0 and v_∞ with $v_0 > v_\infty$. However, as explained in Appendix D, the real positivity constraint [see Eq. (12)] on $g(\omega) = 1 - e^{i\omega l/v(\omega)}$ rules out simple phenomenological expressions for the edge-magnetoplasmon velocity $v(\omega)$. Therefore we shall discuss the ideal $\nu = 1$ case using the long-range model presented in Appendix B.

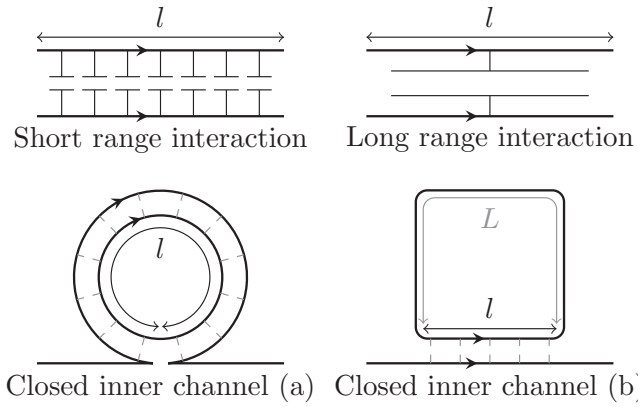


FIG. 6. Schematic view of the main types of interaction discussed at $\nu = 2$. Short-range interaction corresponds to a capacitive coupling between charge densities at the same position in the two channels, and no coupling between different positions. Long-range interaction describes a situation where the system behaves as one big capacitor. We are also interested in situations where the inner channel is closed on itself and interacts with the outer channel either along its whole length (a) or only on a small portion of the closed loop (b). In either of these cases, interactions can be short or long range.

3. The $\nu = 2$ case

The $\nu = 2$ edge channel system is the simplest and experimentally most relevant case involving more than one channel. In this case, two copropagating edge channels separated by approximately 100 nm experience strong intra and inter-channel screened Coulomb interactions. Several models have been developed to describe this situation and are briefly reviewed here.

a. Co-propagating channels with short-range interaction. In the presence of nearby metallic side gates, Coulomb interactions are screened and the charge density in one channel is capacitively coupled to the charge density at the same point in the other channel [18]. More precisely, charge density in channel i at position x and energy ω $\rho_i(x, \omega)$ is coupled to the local electrostatic potential U through distributed capacitances: $\rho_i(x, \omega) = C_{ij}U_j(x, \omega)$. This model, schematically depicted on Fig. 6, is known to give a good description of interactions in experimental systems at small energies, a fact that has been directly probed in the frequency [67] and time [70] domains and indirectly confirmed in Ref. [71]. Within the interaction region, edge-magnetoplasmon eigenmodes are delocalized over the two channels and propagate at different velocities. This leads to the following edge-magnetoplasmon scattering matrix [60]

$$S(\omega) = \begin{pmatrix} p_+ e^{i\omega\tau_+} + p_- e^{i\omega\tau_-} & q(e^{i\omega\tau_-} - e^{i\omega\tau_+}) \\ q(e^{i\omega\tau_-} - e^{i\omega\tau_+}) & p_+ e^{i\omega\tau_-} + p_- e^{i\omega\tau_+} \end{pmatrix}, \quad (16)$$

where

$$p_{\pm} = \frac{1 \pm \cos(\theta)}{2}, \quad q = \frac{\sin(\theta)}{2}, \quad (17a)$$

$$\tau_+ = \frac{l}{v_+}, \quad \tau_- = \frac{l}{v_-}. \quad (17b)$$

In these equations, θ corresponds to the coupling strength, v_+ to the velocity of the slowest mode and v_- to the one of the fastest mode. In the strong-coupling regime, $\theta = \pi/2$, the corresponding modes are a fast charge mode, which is symmetric across both channels and an antisymmetric slow neutral mode [18]. The edge magnetoplasmon transmission coefficient $t(\omega)$ is equal to $S_{11}(\omega)$.

b. Co-propagating channels with long-range interaction. The second model for interacting co-propagating channels assumes that local potentials U are uniform on the whole length of the interaction region. The interaction region is a capacitor (see Fig. 6) and can be discussed in the spirit of the discrete element circuit models introduced by Büttiker *et al.* for quantum conductors [72] and quantum Hall edge channels [73]. This approach leads to the following edge-magnetoplasmon scattering matrix [68]

$$S(\omega) = \begin{pmatrix} p_+ \mathcal{T}_+(\omega) + p_- \mathcal{T}_-(\omega) & q(\mathcal{T}_-(\omega) - \mathcal{T}_+(\omega)) \\ q(\mathcal{T}_-(\omega) - \mathcal{T}_+(\omega)) & p_+ \mathcal{T}_-(\omega) + p_- \mathcal{T}_+(\omega) \end{pmatrix}, \quad (18)$$

where p_{\pm} and q are given by Eq. (17) and other parameters are given in terms of the dimensionless parameter $x = \omega l / v_F$ by

$$\mathcal{T}_{\pm}(\omega) = \frac{e^{ix} - 1 + i\alpha_{\pm} x e^{ix}}{e^{ix} - 1 + i\alpha_{\pm} x} \quad (19)$$

with α_{\pm} being linked to the eigenvalues of the capacitance matrix C_{\pm} by $\alpha_{\pm} = R_K C_{\pm} v_F / l$. Here also, $t(\omega) = S_{11}(\omega)$ where this time, $S(\omega)$ is given by (18) and (19).

4. The $\nu = 2$ case with a loop

Figure 6(a) also depicts another situation that can be built with two copropagating edge channels, where the inner one is closed on itself over the length l where interaction takes place [34]. In the geometry depicted on Fig. 6(b), the same idea of a closed inner channel is used, but the copropagating distance over which interaction takes place is only a part of the total length of the loop. Such a geometry has been used for mitigating decoherence in electronic Mach-Zehnder interferometers [35]. Both geometries impose a periodicity condition on the field for the inner channel:

$$\phi_2(0, \omega) = \phi_2(l, \omega) e^{i\omega\tau_L}, \quad (20)$$

where $\tau_L = L/v_+$ is the time it takes for an excitation to cover the noninteracting length L of the loop. The transmission coefficient is then obtained in full generality as

$$t(\omega) = S_{11}(\omega) + \frac{S_{12}(\omega)S_{21}(\omega)}{e^{-i\omega\tau_L} - S_{22}(\omega)}, \quad (21)$$

where $S(\omega)$ is the scattering matrix describing the region of the loop over which the two channels interact with each other. As expected, in the absence of dissipation, we have a unitary S matrix and this transmission coefficient has a modulus of 1. In the case of short-range interaction, the scattering matrix is given by Eq. (18) and the last equation specializes to

$$t(\omega) = -e^{i\omega(\tau_+ + \tau_- - \tau_L)} \left(\frac{e^{i\omega\tau_L} - p_+ e^{-i\omega\tau_+} - p_- e^{-i\omega\tau_-}}{e^{-i\omega\tau_L} - p_+ e^{i\omega\tau_+} - p_- e^{i\omega\tau_-}} \right). \quad (22)$$

Of course, the special case (a) is recovered for $\tau_L = 0$.

III. ELECTRONIC DECOHERENCE

Let us now explain how to obtain the outgoing electronic coherences assuming a single-electron excitation is injected into the interaction region. Let us stress that this computation relies on the bosonization formalism that assumes an electronic linear dispersion relation, a valid approximation so far for electron quantum optics experiments. We will first review the main steps and the essential points of the general method developed for comparing the electronic decoherence of Landau and Levitov quasiparticles [33]. Then, we will discuss in details decoherence within a dissipationless single edge channel ($\nu = 1$) and then in the $\nu = 2$ edge channel system. Our computations are performed at zero temperature to enlighten the underlying physics of electronic decoherence. Moreover, in experiments performed on Landau excitations, temperature effects have been shown to be quite small [15].

A. General results

The key point is that the fermionic operators can be expressed in terms of the bosonic operators by [74,75]

$$\psi_\alpha(x, t) = \frac{\mathcal{U}_\alpha}{\sqrt{2\pi a}} \exp(i\sqrt{4\pi}\phi_\alpha(x, t)), \quad (23)$$

where α the channel index, a an ultraviolet cutoff that gives the length scale below which bosonization is not valid and \mathcal{U}_α (respectively, $\mathcal{U}_\alpha^\dagger$) is the Klein operator suppressing (respectively, adding) one electron from the reference vacuum into edge channel α .

In the bosonization framework, the interaction region is a frequency dependent beam splitter for the edge-magnetoplasmon modes. An incoming coherent state for these modes is scattered exactly as a classical electromagnetic wave on an optical beam splitter [68]. More precisely, an incoming coherent edge magnetoplasmon of the form $|\Lambda_1\rangle \otimes |\Lambda_2\rangle$ is transformed into an outgoing state $|\Lambda'_1\rangle \otimes |\Lambda'_2\rangle$ where for all $\omega > 0$, $\Lambda'_\alpha(\omega) = \sum_\beta S_{\alpha\beta}(\omega)\Lambda_\beta(\omega)$. Because Eq. (23) shows that single-electron states are described as quantum superposition of coherent edge-magnetoplasmon states, an exact description of the outgoing state after the interaction region can be obtained.

More precisely, a single-electron state injected in edge channel 1 corresponds, with the notations given in Appendix A, to

$$|\varphi_e, F\rangle_1 \otimes |F\rangle_2 = \int_{-\infty}^{+\infty} \varphi_e(t) \frac{\mathcal{U}_1^\dagger}{\sqrt{2\pi a}} \bigotimes_{\omega>0} (|\Lambda_\omega(t)\rangle_1 \otimes |0_\omega\rangle_2) dt \quad (24)$$

and comes out of the interaction region as

$$\int \varphi_e(t) \frac{\mathcal{U}_1^\dagger}{\sqrt{2\pi a}} \bigotimes_{\omega>0} (|t(\omega)\Lambda_\omega(t)\rangle_1 \otimes |r(\omega)\Lambda_\omega(t)\rangle_2) dt. \quad (25)$$

In this equation, we adopt the convention used in the remaining of this text that $S_{11}(\omega) = t(\omega)$ and $S_{21}(\omega) = r(\omega)$, other coefficients of S being irrelevant as no injection is made in channel 2. Tracing on the second edge channel degrees of freedom leads to the reduced outgoing many-body density

operator for the injection edge channel [32]:

$$\rho_1 = \int \varphi_e(t)\varphi_e^*(t') \mathcal{D}_{\text{ext}}(t-t') \psi_1^\dagger(t)|g_1(t)\rangle \times \langle g_1(t')|\psi_1(t') dt dt', \quad (26)$$

where $\mathcal{D}_{\text{ext}}(t-t') = \langle \mathcal{E}_2(t')|\mathcal{E}_2(t)\rangle$ is the extrinsic decoherence coefficient corresponding to the overlap of imprints

$$|\mathcal{E}_2(t)\rangle = \bigotimes_{\omega>0} |r(\omega)\Lambda_\omega(t)\rangle \quad (27)$$

left in the second edge channel by localized electrons injected in the first edge channel at times t and t' . It is given by [32]

$$\mathcal{D}_{\text{ext}}(\tau) = \exp\left(\int_0^{+\infty} |r(\omega)|^2 (e^{i\omega\tau} - 1) \frac{d\omega}{\omega}\right). \quad (28)$$

The coherent edge-magnetoplasmon state $|g_1(t)\rangle$ in Eq. (26) corresponds to the cloud of electron/hole pairs generated by Coulomb interactions when a localized electron $\psi^\dagger(t)|F\rangle$ goes through the interaction region:

$$|g_1(t)\rangle = \bigotimes_{\omega>0} |(1-t(\omega))\Lambda_\omega(t)\rangle. \quad (29)$$

In the same way, in the $\nu = 2$ case, the reduced density operator for the inner edge channel can be obtained by tracing out over the outer edge channel. This leads to

$$\rho_2 = \int \varphi_e(t)\varphi_e(t') \mathcal{D}_{\text{inj}}(t-t') |\mathcal{E}_2(t)\rangle \langle \mathcal{E}_2(t')| dt dt', \quad (30)$$

in which the state $|\mathcal{E}_2(t)\rangle$ is defined by Eq. (27) and in which the decoherence coefficient

$$\mathcal{D}_{\text{inj}}(\tau) = \exp\left(\int_0^{+\infty} |t(\omega)|^2 (e^{i\omega\tau} - 1) \frac{d\omega}{\omega}\right), \quad (31)$$

where ‘‘inj’’ stands for injection channel, is equal to the overlap $\langle \mathcal{E}_1(t)|\mathcal{E}_1(t+\tau)\rangle$ of the outgoing states of the injection edge channel corresponding to two different electron injection times:

$$|\mathcal{E}_1(t)\rangle = \bigotimes_{\omega>0} |t(\omega)\Lambda_\omega(t)\rangle. \quad (32)$$

This many-body description then gives access to all electronic coherence functions after the interaction region.

B. Computing single-electron coherences

Let us now turn to first-order coherences in the outer and inner channels after interaction, denoted, respectively, by $\mathcal{G}_{\text{out},1}^{(e)}(t|t')$ and $\mathcal{G}_{\text{out},2}^{(e)}(t|t')$.

1. Outer channel coherence

When computing $\mathcal{G}_{\text{out},1}^{(e)}(t|t')$, the final results appear as a sum of two terms. The first one corresponds to a modification of the Fermi sea which, under the right condition, can be seen as the contribution of electron-hole pairs generated by Coulomb interaction vacuum state (namely the Fermi sea). This one is called the *modified vacuum*. The second contribution comes from the incoming excitation elastically scattered or after interaction induced relaxation. This one is called the *wave packet* contribution. Generically, these two contributions

overlap in the Wigner function representation and thus cannot be accessed separately. However, as explained in Ref. [32], when the coupling to the environment is sufficiently weak and the incoming electronic excitation is injected as sufficiently high energy so that it does not relax down to the Fermi sea, these two contributions do not overlap since the first one contributes around the Fermi level whereas the latter one contributes only within a limited bandwidth below the injection energy. In this dynamical Coulomb blockade-like regime discussed in Appendix E, low-energy electron/hole excitations are part of the electromagnetic effective environment seen by the incoming single-electron excitation.

In full generality, these two contributions can be written as [33]

$$\mathcal{G}_{\text{MV},1}^{(e)}(t|t') = \int \varphi_e(t_+) \varphi_e^*(t_-) \mathcal{D}(t, t', t_+, t_-) \times \langle \psi^\dagger(t') \psi(t) \rangle_F \langle \psi(t_-) \psi^\dagger(t_+) \rangle_F dt_+ dt_-, \quad (33a)$$

$$\mathcal{G}_{\text{WP},1}^{(e)}(t|t') = \int \varphi_e(t_+) \varphi_e^*(t_-) \mathcal{D}(t, t', t_+, t_-) \times \langle \psi(t) \psi^\dagger(t_+) \rangle_F \langle \psi(t_-) \psi^\dagger(t') \rangle_F dt_+ dt_-, \quad (33b)$$

where

$$\mathcal{D}(t, t', t_+, t_-) = \gamma_+(t_+ - t') \gamma_-(t_+ - t) \times \gamma_+^*(t_- - t) \gamma_-^*(t_- - t') \quad (34)$$

is the effective single-particle decoherence coefficient, which takes into account both the action of environmental degrees of freedom and of electron-hole pairs cloud created in the injection channel. It is determined by the two functions

$$\gamma_\pm(t) = \exp\left(\pm \int_0^\infty \frac{d\omega}{\omega} (1 - t(\omega)) (e^{i\omega t} - 1)\right). \quad (35)$$

Explicit expressions for the two contributions (33a) and (33b) in the frequency domain are given in Ref. [[33], Supplementary Material] and form the starting point of the numerical evaluation of the outgoing electronic coherence in the frequency domain (see Sec. III B 3).

A physically important quantity is the elastic scattering amplitude $\mathcal{Z}(\omega)$ for an incoming single-electron excitation at energy $\hbar\omega > 0$. It determines the inelastic scattering probability $\sigma_{\text{in}}(\omega) = 1 - |\mathcal{Z}(\omega)|^2$ for an electron flying across the interaction region. This quantity is crucial for discussing the fate of a single electronic quasiparticle. Considering an incoming single-electron coherence injected at a given quasienergy $\varepsilon > 0$ above the Fermi level, the behavior of $\sigma_{\text{in}}(\varepsilon/\hbar, l)$ as a function of the length of the interaction region l tells us how much of the original quasiparticle has survived after propagation over a distance l . If for $l \gtrsim l^*(\varepsilon)$, $\sigma_{\text{in}}(\varepsilon/\hbar, l)$ is close to unity, meaning that the injected quasiparticle has experienced inelastic scattering, then $\tau_\varphi(\varepsilon) = l^*(\varepsilon)/v_F$ can be interpreted as the lifetime of the quasiparticle injected at $\varepsilon > 0$ above the Fermi level. This enables discussing the Fermi or non-Fermi liquid behavior of quantum Hall edge channels with respect to the fate of a single-electron excitation. For a Fermi liquid, it is expected that, at low energies compared

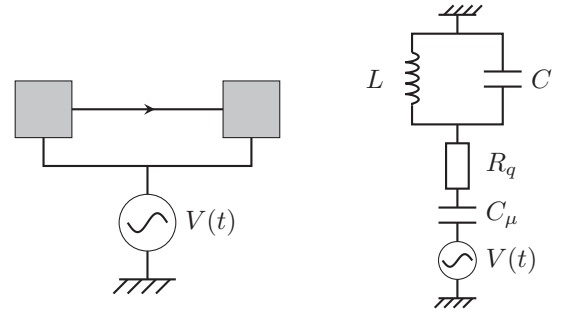


FIG. 7. (Left) Effective dipole associated with the interaction region. (Right) Equivalent effective ZC circuit at low-frequency. The resistive part of $Z(\omega)$ is the relaxation resistance $R_q = R_K/2$ and its imaginary part comes from an LC circuit.

to the Fermi energy, $\tau_\varphi(\varepsilon)$ scales as $1/\varepsilon^2$ thus making the electronic quasiparticle more and more well defined as $\varepsilon \rightarrow 0$. On the other hand, a $1/\varepsilon$ scaling would be the sign of the breakdown of a well defined electronic quasiparticle close to the Fermi level.

Within our framework, the elastic scattering amplitude $\mathcal{Z}(\omega)$ is obtained as [32]

$$\mathcal{Z}(\omega) = 1 - \int_0^\omega B_-(\omega') d\omega', \quad (36)$$

where B_- is defined as the regular part of the Fourier transform of γ_- and therefore satisfies the integral equation

$$\omega B_-(\omega) = t(\omega) - 1 + \int_0^\omega B_-(\omega') (t(\omega - \omega') - 1) d\omega' \quad (37)$$

with initial condition $B_-(0^+) = -\frac{dt}{d\omega}(\omega = 0^+)$. Equations (36) and (37) pave the way towards a perturbative expansion of $\mathcal{Z}(\omega)$ as a sum of convolutions of $(1 - t(\omega))/\omega$, which is well suited to the low-frequency expansion of the finite frequency admittance $g(\omega) = 1 - t(\omega)$. At second order in $\omega R_K C_\mu$,

$$g(\omega) \simeq -iC_\mu R_K \omega + \frac{R_q}{R_K} (\omega R_K C_\mu)^2, \quad (38)$$

where C_μ and R_q , respectively, denote the electrochemical capacitance and the relaxation resistance of the interaction region in the discrete circuit element representation depicted on the right panel of Fig. 7. Substituting this expansion into Eqs. (36) and (37) then leads to the lowest nontrivial order [76]:

$$\sigma_{\text{in}}(\omega) \simeq \left(\frac{R_q}{R_K} - \frac{1}{2}\right) (\omega R_K C_\mu)^2. \quad (39)$$

This is dominant contribution to the inelastic scattering probability when $R_q > R_K/2$, that is when the edge channel under contribution is coupled to environmental edge channels whose dissipation adds up to the single edge channel relaxation resistance $R_K/2$. As we shall see in Sec. III C, for a single-electron excitation injected into a single dissipationless edge channel, the inelastic scattering probability scales as $(\omega R_K C_\mu)^6$. Consequently, at fixed l , the electronic quasiparticle does survive flying across a finite length interaction region, an expected

result since in the limit $\varepsilon \rightarrow 0$ at a fixed l , the dominant physics is the one imposed by the reservoir, i.e., the Fermi liquid physics. As we shall see in a forthcoming section, taking the limit in the reverse order (increasing l at fixed $\varepsilon > 0$) does not lead to the same conclusion.

2. Inner channel coherence

Using the reduced density matrix ρ_2 for the inner channel, any coherence function we are interested in can be computed. The main result is strikingly simple: $\mathcal{G}_{\text{out},2}^{(e)}(t|t')$ is of the same exact form as $\mathcal{G}_{\text{MV},1}^{(e)}(t|t')$ if we replace the function $t(\omega)$ in the decoherence coefficient with $1 + r(\omega)$. The fact that there is no wave packet term emphasizes that no electron has been injected into the inner channel: only a cloud of electron/hole pairs is created.

3. Numerical method

As shown in Ref. [[33], Supplementary Material], the numerical evaluation consists in evaluating multiple integrals of factors. The implementation is quite straightforward, even though the main difficulty comes from the number of nested integrals (four for each point of the electronic coherence). For this, we use a frequency representation of the coherence. We discretize the input coherence on a grid using two directions, ω and $\delta\omega$. ω is the conjugate of $t - t'$ and thus encodes the frequency dependence in the Wigner function. $\delta\omega$ is the conjugate of $(t + t')/2$, and thus gives access to time dependence in the Wigner function. When there are n points in the input coherence in each direction ω and $\delta\omega$, a naive implementation would require an $\mathcal{O}(n^6)$ computation time. However, by exploiting the structure of the expressions, we have been able to lower the total complexity to $\mathcal{O}(m \times n^4)$ where n denotes the number of points in the direction ω and m the number of points in the direction $\delta\omega$. This structure allows us to decouple the two directions and, as such, we can have a better numerical evaluation by lowering the discretization step in the direction ω , without touching to the direction $\delta\omega$, as long as we have enough information about the time evolution of the Wigner function. With these refinements and using the OpenMP parallel framework, a post-interaction coherence is computed within five to ten minutes on a 64 cores computer.

Discretization steps are chosen by looking at errors. The trace of the excess single-electron coherence is the total charge injected and should not change. If this already very sensitive indicator is not enough, we compute the average outgoing electric current from the outgoing excess single-electron coherence and compare it to its value obtained by applying edge-magnetoplasmon scattering to the incoming average current. All graphs presented in the following exhibit errors smaller than 5% for those tests.

C. Decoherence at $\nu = 1$

1. General picture

Let us first discuss electronic decoherence by using a crude physical picture for a single edge channel in which we have a low-frequency edge-magnetoplasmon velocity v_0 greater than the high-frequency velocity v_∞ . Let us denote by ω_c the crossover frequency between these two velocity regimes. In

the model presented in Sec. II C 2, $\omega_c \simeq 2\pi v_F/l$ as can be seen from Fig. 5.

At low energies $\omega \ll \omega_c$, electronic decoherence arises from the ω dependence of the edge-magnetoplasmon velocity or, equivalently of the finite frequency admittance $g(\omega)$. At low enough frequencies, the interaction region of the ideal single channel can also be described in terms of discrete circuit elements such as its electrochemical capacitance C_μ , its relaxation resistance is equal to [72] $R_q = R_K/2$ and $R_K C_\mu$ is the time of flight l/v_0 of the low-frequency edge magnetoplasmons. Understanding electronic decoherence thus requires describing the extra-reactance part of $g(\omega)$, the simplest description of which is an LC oscillator as on Fig. 7. The circuit parameters L and C can then be expressed in terms of the parameters of the effective model used to describe the $\nu = 1$ ideal edge channel (see Appendix C):

$$\frac{L/R_K}{R_K C_\mu} = \frac{1 + 4\alpha}{12}, \quad (40a)$$

$$\frac{C}{C_\mu} = \frac{1 + 4\alpha}{5}. \quad (40b)$$

Then, as explained in Appendix F, the inelastic scattering probability can be expanded into powers of $\omega R_K C_\mu$. This results in the dominant behavior for the inelastic scattering probability when $R_q = R_K/2$:

$$\sigma_{\text{in}}(\omega) \simeq \frac{11}{180} \left(\frac{L/R_K}{R_K C_\mu} - \frac{1}{12} \right)^3 (\omega R_K C_\mu)^6, \quad (41)$$

in terms of the discrete element circuit description of Fig. 7. In the specific model used here, L and C are given by Eqs. (40). As expected, since no energy can be emitted within external environmental channels, the inelastic scattering probability scales much more rapidly towards zero in the limit $\omega R_K C_\mu \rightarrow 0$ than when external dissipation is present [see Eq. (39) where $R_q > R_K/2$].

Let us now turn to electrons injected at high energy. Since, for $\omega \gtrsim \omega_c$, edge magnetoplasmons travel at a velocity close to v_∞ , decoherence mostly arises from the effective edge-magnetoplasmon scattering phase $\tilde{t}(\omega) = t(\omega)e^{-i\omega\tau_\infty}$, which is roughly 1 for $\omega \gtrsim \omega_c$ and $e^{-i\omega\Delta\tau}$ for $\omega \lesssim \omega_c$, where $\Delta\tau = \tau_\infty - \tau_0$ denotes the difference of time of flights between high- and low-energy edge magnetoplasmons. As interactions have an effective bandwidth $\sim \omega_c$, we expect the creation of electron/hole pair excitations to happen within one to a few ω_c around the Fermi level. Consequently, for electronic excitations injected at a much higher energy, the corresponding low-energy edge-magnetoplasmon modes can be viewed as an effective distinct environment for the high-energy electronic excitations [32].

In this dynamical Coulomb blockade like regime, discussed more precisely in Appendix E, the incoming electron loses energy through electron/hole pair creation within a few $\hbar\omega_c$ of the Fermi sea. The low-energy electron/hole pairs will then propagate along at the low-energy edge-magnetoplasmon velocity. In a first approximation, the physical picture for the decoherence and relaxation of single-electron excitations injected at high energy thus involves the incoming electron and its relaxation tail [described by Eq. (E6)] propagating

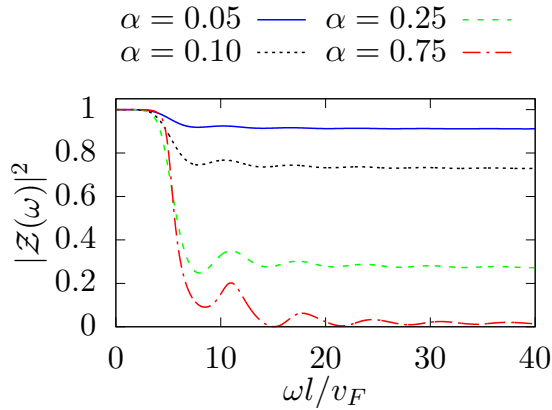


FIG. 8. Elastic scattering probability for a single-electron excitation as a function of $\omega l/v_F$ for the long-range interaction model given by Eq. (B5), for different values of the coupling constant α .

at the high-energy velocity v_∞ and the corresponding low-energy electron/hole pairs propagating at the low-energy edge-magnetoplasmon velocity v_0 . This simple picture justifies interpreting v_∞ as the velocity of hot electrons whereas v_0 is viewed as a plasmon velocity.

The important question is then to determine what part of the initial quasiparticle survives in the large l limit. The answer, derived in Appendix E is the elastic scattering probability for an electron injected at very high energy, or equivalently the large l limit of $|\mathcal{Z}(\omega)|^2$ for $\omega l/v_F \gg 2\pi$ for fixed $\omega > 0$:

$$Z_\infty = \exp\left(-\int_0^{+\infty} |1 - \tilde{t}(\omega)|^2 \frac{d\omega}{\omega}\right). \quad (42)$$

This quantity which, in the long-range model of Sec. IIC2 only depends on the effective coupling constant α , represents the survival probability of the single-electron excitation injected at energy $\varepsilon > 0$ above the Fermi level once it has propagated over a distance larger than $l^*(\varepsilon) = hv_F/\varepsilon$.

2. Numerical results at $\nu = 1$

Let us now illustrate this discussion by using an ω -dependent unit modulus transmission $t(\omega)$ given by the long-range interaction model for $\nu = 1$. We will discuss both the case of a strong-coupling material ($\alpha = 0.75$) and of a weak-coupling material ($\alpha \simeq 0.05$).

Figure 8 presents the elastic scattering probability $|\mathcal{Z}(\omega)|^2$ as a function of $\omega R_K C_\mu = \omega l/v_0$ for these two values of the coupling constant as well as for intermediate values $\alpha = 1/10$ and $\alpha = 1/4$. At strong coupling, the low-energy almost flat plateau close to unity is followed by a very strong decay of $|\mathcal{Z}(\omega)|^2$ when $\omega R_K C_\mu \gtrsim 2\pi$ towards a very small value. The low-coupling case also leads to a decay of the elastic scattering probability when $\omega R_K C_\mu \gtrsim 2\pi$ but towards a higher value, $Z_\infty \simeq 0.9$.

Figure 9 depicts the asymptotic value Z_∞ of the elastic scattering probability $|\mathcal{Z}(\omega)|^2$ at high energy as a function of the coupling constant α in the model of Sec. IIC2. We clearly see the difference between weak and strong coupling on electronic decoherence of high-energy excitations; for $\alpha = 0.05$, $Z_\infty \simeq 0.91$, whereas for $\alpha = 0.75$, $Z_\infty \simeq 0.015$.

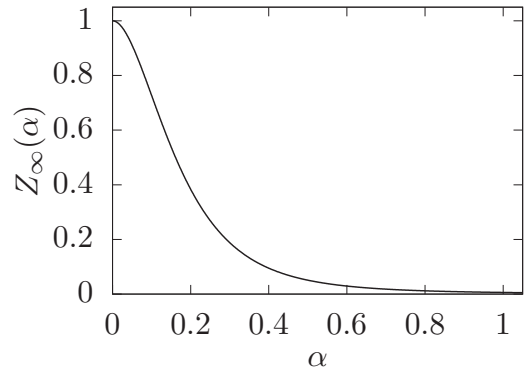


FIG. 9. Asymptotic elastic scattering probability for high energy electrons $Z_\infty(\alpha)$ given by Eq. (42) as a function of the coupling constant α for the model introduced in Sec. IIC2.

Let us now turn to the low-energy regime: Fig. 10 depicts the ratio of the full inelastic scattering probability to the perturbative expression as a function of ω . It shows that the perturbative result is only valid at low energies, that is significantly before the drop of the elastic scattering probability, when the inelastic scattering probability is still very close to unity. Understanding the full behavior of the elastic scattering probability indeed requires a full non perturbative approach even at weak coupling because, at higher injection energies, multiple low-energy electron/hole pair emissions coexist with the emission of single electron/hole pair of higher energy. Properly accounting for all these processes requires the full knowledge of the frequency dependence of $g(\omega)$ for which the simplest discrete element circuit descriptions are not sufficient.

Figure 11 presents the electronic decoherence of an incoming wave packet injected at energy $\omega_0 R_K C_\mu = 15$. In the weak coupling case (lower panel), we clearly see the separation in energy between the elastically scattered electronic excitation together with its relaxation tail at high energy and the resulting electron/hole pairs close to the Fermi level. This is expected since the elastic scattering probability is quite high at the injection energy. The temporal separation

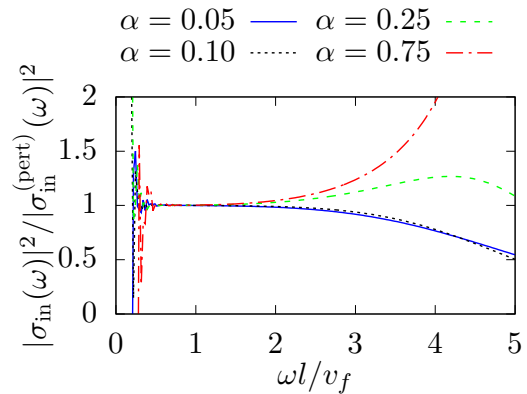


FIG. 10. Ratio of inelastic scattering probabilities for the full model to its perturbative circuit expansion (F1) at low energy. Numerical errors at small $\omega l/v_F$ are due to the rapid decay of the dominant $(\omega l/v_F)^6$ asymptotic behavior of the inelastic scattering probability at very low energies.

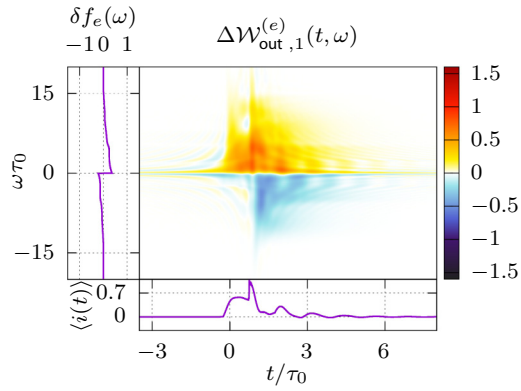


FIG. 11. Wigner distribution function of an incoming wave packet injected at energy $\omega_0 R_K C_\mu = 15$. Top panel: outgoing single-electron coherence for $\alpha = 0.75$. (Bottom) Outgoing single-electron coherence for $\alpha = 0.05$. $t = 0$ corresponds to the expected time of reception for a free propagation at the low-energy velocity v_0 .

which is a result of the difference between the hot-electron velocity v_∞ and the plasmon velocity v_0 is also clearly visible on the average electric current $\langle i(t) \rangle$: the sharp rise of the current corresponds to the arrival of the elastically scattered quasiparticle and $t = 0$ corresponds to propagation at the fastest velocity v_0 .

By contrast, in the strong-coupling case (upper panel), electronic decoherence is much stronger. The relaxation tail of the incoming excitation is visible as a sharp rise of the current which arrives later than the beginning of the neutral electron/hole pair cloud. As expected the difference between the plasmon and high-energy electron velocities is also more important than in the weak-coupling case but we also see that the weight of the electron/hole cloud contribution in the average electrical current is much more important than at weak coupling.

These results can be compared to the ones depicted on Fig. 12 presenting the electronic decoherence of an incoming wave packet injected at $\omega_0 R_K C_\mu \simeq 3$, an energy lower than the previously discussed threshold. Most of its spectral weight is below the threshold. The Landau quasiparticle propagates without experiencing much decoherence in both cases. We also see that it propagates at the low-energy edge-magnetoplasmon velocity v_0 . As expected, the incoming excitation seems less altered at weak coupling ($\alpha = 0.05$, lower panel) than at strong coupling ($\alpha = 0.75$, upper panel).

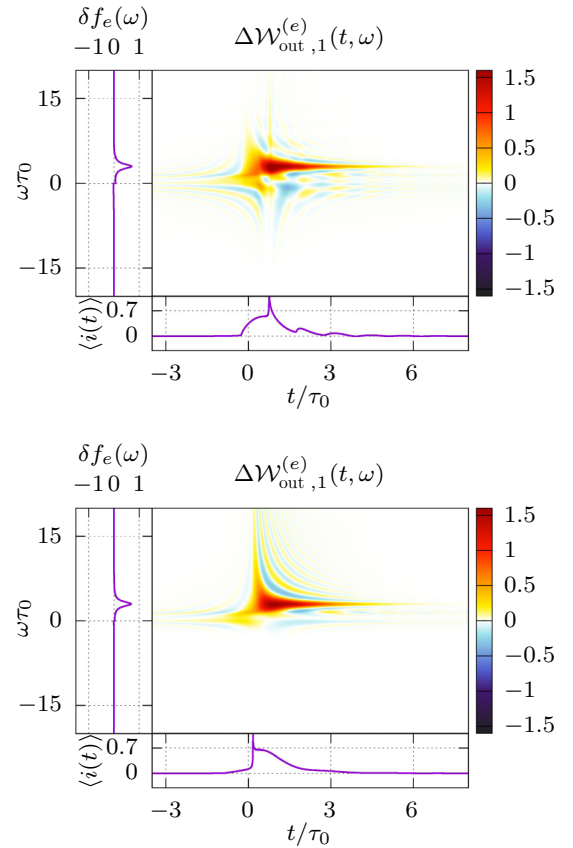


FIG. 12. Wigner distribution function of an incoming wave packet injected at energy $\omega_e R_K C_\mu = 3$. Top panel: outgoing single-electron coherence for $\alpha = 0.75$. (Bottom) Outgoing single-electron coherence for $\alpha = 0.05$. $t = 0$ is the expected time of reception for a free propagation at the low-energy velocity v_0 .

The bottom line of this discussion is that, at strong coupling, the injected single-electron quasiparticle at a given energy above the Fermi level gets destroyed with a very high probability ($Z_\infty \gg 1$) after propagating over a distance that scales as $1/\varepsilon$. By contrast, at weak coupling, Z_∞ is close to unity and the quasiparticle still makes sense in the thermodynamic limit ($l \rightarrow +\infty$ and $\varepsilon > 0$ fixed). Therefore, by looking at the quasiparticle decay in this limit, we see that increasing the effective coupling α brings us closer to a non-Fermi liquid behavior in which we expect $Z_\infty = 0$ in the large l limit $l \gg l^*(\varepsilon) \sim 1/\varepsilon$.

On the other hand, the ground-state electronic Green's function is left unaltered in the infrared limit, thus leaving intact the jump in the electronic distribution function at the Fermi energy. This is to be contrasted with the Luttinger liquid [11], where an algebraic singularity is expected.

As reviewed in Sec. II A 2, a convenient tool for testing robustness to decoherence in electron quantum optics is the Hong-Ou-Mandel experiment [77,78]. One expects strong and weak coupling regimes to lead to quantitatively different results in this experiment. We have thus computed the HOM signal Δq defined by Eq. (8) in both cases. Results are shown in Fig. 13 for both injection energies and both coupling values. As discussed on the Wigner functions, these curves

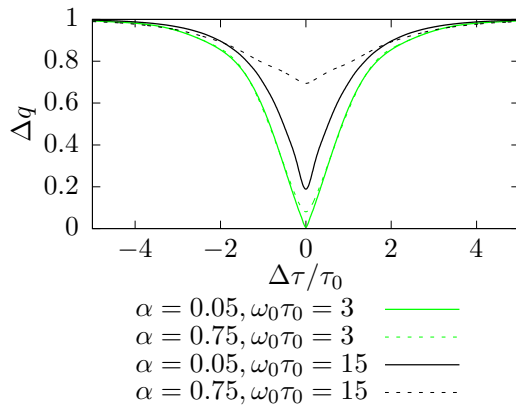


FIG. 13. Theoretical results of an Hong-Ou-Mandel interferometry experiment obtained from the Wigner functions displayed in Figs. 11 and 12. As expected from the Wigner functions themselves, low-energy excitations ($\omega_0\tau_0 = 3$) present a high-contrast HOM dip. The results for high-energy excitations ($\omega_0\tau_0 = 15$) show the difference between a weak coupling ($\alpha = 0.05$) and a strong coupling ($\alpha = 0.75$) material.

confirm that weak coupling materials would lead to a stronger protection against decoherence.

3. Commenting on AlGaAs/GaAs vs graphene.

As mentioned in Sec. II C 2, exfoliated graphene on a silicon oxide surface may correspond to a weak coupling value of α and thus to a much lower electronic decoherence. Moreover, provided velocities in graphene are much higher than in AlGaAs/GaAs, the crossover energy between the low- and high-energy regimes should be much higher for fixed device dimensions. For example, a $l = 20 \mu\text{m}$ propagation distance corresponds to $\omega/2\pi = v_F/l \simeq 500 \text{ GHz}$ for $v_F = 10^6 \text{ m s}^{-1}$ and to 50 GHz for $v_F = 10^5 \text{ m s}^{-1}$.

The single-electron source based on the mesoscopic capacitor [20] that has been developed in AlGaAs generates single-electron excitations at an energy comparable to this crossover scale. With our estimated parameters, strong electronic decoherence is expected for a propagation above $30 \mu\text{m}$ when injecting at an energy of the order of $40 \mu\text{eV}$.¹ Although no single-electron source has been developed yet for graphene in the quantum Hall regime, the ratio of estimated high-energy velocities in the two materials suggests a propagation distance of the order of $200 \mu\text{m}$ in a $\nu = 1$ ideal channel before any significant step in the inelastic scattering probability manifests itself in graphene. Moreover, as discussed in the previous section, even for such long propagation distances, electronic decoherence would be much lower in a weak coupling material compared to the case of a strong coupling material (see Fig. 9).

¹These figures correspond to the ideal $\nu = 1$ case, which is not the case that has been experimentally studied. In the experiments, extrinsic decoherence induced by the second edge channel leads to much shorter coherent propagation distance for such energy resolved excitations.

Of course, this discussion has been made within the framework of our model for electronic propagation within an ideal $\nu = 1$ edge channel. In practice, it is known that edge magnetoplasmons propagating along quantum Hall edge channels experience dissipation [67,69,79–81]. This is one of the possible causes for the missing energy in electronic relaxation experiments [60]. Investigating edge-magnetoplasmon dissipation effects on single-electron decoherence is certainly very important but this would go beyond the scope of the present paper. Nevertheless, we think that the effect of the Fermi velocity difference on the coupling constant and on the length to time scale conversion may lead to important differences between strong and weak-coupling materials concerning single-electron decoherence. As suggested by Fig. 13, HOM experiments may offer clear discriminating signatures of weak versus strong coupling materials but this would require the experimental development of single electron sources for Landau quasiparticles injection in graphene quantum Hall edge channels.

Finally, let us mention that a Mach-Zehnder interferometer has recently been demonstrated with encapsulated monolayer graphene sheet embedded within hexagonal boron nitride [82]. The beam splitters exploit same-spin intervalley scattering at a pn junction and the interferometer's geometry is controlled by Coulomb exchange interactions. Surprisingly, a contrast of 90% has been observed at low bias in a parameter regime where one arm consists of one carrier edge channel and the other of two and for an arm length of $1.2 \mu\text{m}$. Such a high contrast remains up to a bias voltage larger than $200 \mu\text{V}$. Although decoherence mechanisms have not been yet studied in great detail for this device, we think that such a surprisingly high contrast together with our discussion of coupling constant and high-energy velocity effects calls for intensive studies of single-electron decoherence in a material such as graphene.

D. Decoherence at $\nu = 2$

Let us now turn to the $\nu = 2$ case, which has already been studied in relation with experiments [33,83]. In the present case, we shall briefly recall the results obtained using the dispersionless model for edge-magnetoplasmon scattering between two strongly coupled copropagating edge channels (short-range interactions in Sec. II C 3) before discussing the influence of the finite range of interactions in an Hong-Ou-Mandel experiment.

1. Short-range interactions

Numerical results for both outer and inner channel coherences in the specific case of short-range interaction at strong coupling are presented in Fig. 14 for the Leviton source and in Fig. 15 for a Landau excitation. Two distinct behaviours can be seen on these results. In the case of the Leviton source, the emitted state is a coherent state of plasmons created by the application of a classical voltage drive to an Ohmic contact. Its evolution is dominated by fractionalization: we observe a simple separation of the incoming packet into two modes, one symmetric over the two channels and the other antisymmetric (see Fig. 14). In the outer channel, we recover exactly a fractionalization of the incoming excitation into two Levitons

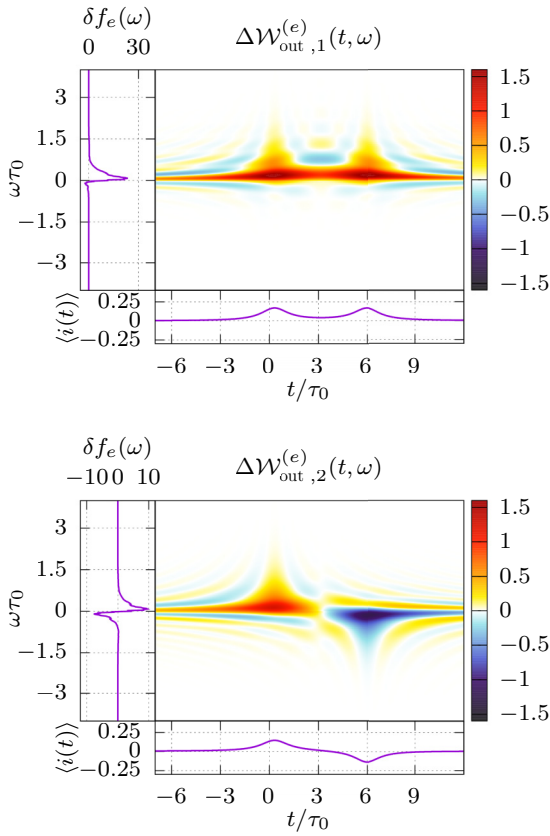


FIG. 14. Wigner function for the outer (top) and inner (bottom) channels for a Leviton excitation of width τ_0 . We use short-range interaction with parameters $\theta = \pi/2$, $\tau_+ = 6\tau_0$ and $\tau_- = \tau_+/20$. Since we inject a coherent state of plasmons, it fractionalizes into half-excitations and exhibits the behavior of spin-charge separation, with the apparition of a fast symmetric mode over the two channels mode and a slow antisymmetric one.

with charges $-e/2$, as was predicted in various theoretical works [68,84] and demonstrated experimentally [16,67,85].

As recalled in Sec. II B, a Landau type excitation illustrates a different scenario: before fractionalization takes place, many-body decoherence leads to a fast energy relaxation with a strong decay of the weight around the injection energy, as can be seen on the upper panel of Fig. 15. This theoretical scenario and the corresponding quantitative predictions [33,83] have recently been confirmed by experiments [15]. The lower panel of Fig. 15 shows the electronic coherence in the inner channel. Although most excitations are created close to the Fermi level, we also see excitations created around the injection energy (for electrons) and close to the opposite (for the holes), which are the inner channel equivalent of the elastically scattered part still present in the outer channel.

Before moving on to the long-range interaction model, let us stress that, here Z_∞ is exactly zero as can be seen from many references [18,19,32,33]. An electronic quasiparticle injected at energy $\varepsilon > 0$ above the Fermi level will not survive propagating in the thermodynamic limit. The inelastic scattering probability $\sigma_{\text{in}}(\varepsilon)$ is close to unity as soon as $l \gtrsim l^*(\varepsilon) = \hbar v_s/\varepsilon$. As noticed in Ref. [14], a chiral edge channel propagating along a second one to which it is capacitively

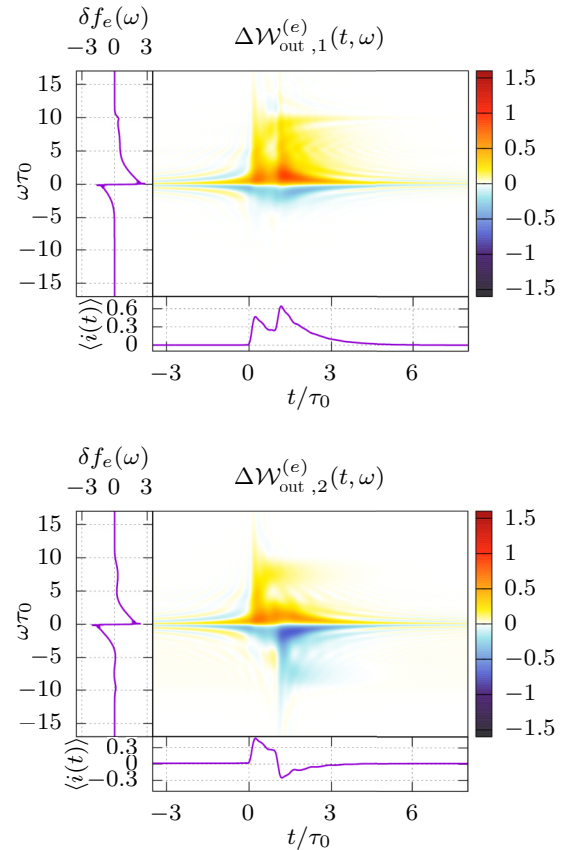


FIG. 15. Wigner function for the outer (top) and inner (bottom) channels for a Landau excitation with parameters $\omega_0\tau_0 = 10$. Interaction parameters are $\theta = \pi/2$, $\tau_+ = \tau_0$, and $\tau_- = \tau_+/20$. In that case, the incoming state is a superposition of coherent plasmonic states. Interactions lead to the destruction of coherences between those states, and the end result is therefore a statistical mixture of coherent plasmonic states, whose energy content is no more resolved around ω_0 . In the time domain, since all bosonic states exhibit spin-charge separation when they pass through the interaction region, we recover once again this type of separation for the electric current.

coupled by an effective short-range interaction is not a Fermi liquid with respect to the fate of the electronic quasiparticle whose lifetime scales as $1/\varepsilon$. Nevertheless, note that, as for the $\nu = 1$ case and contrary to the Luttinger liquid, there is no algebraic singularity in the electronic occupation number of the ground state at the Fermi level.

2. Long-range interactions

At $\nu = 2$, a long-range interaction model can be studied (see Sec. II C 3) and may be experimentally relevant at higher energies [67]. The outgoing Wigner functions for excitations crossing a long-range interaction region are shown on Fig. 16. Several qualitative differences with the short-range case can be observed. First, we see nonvanishing coherence and current at negative times, the reference being given by the time taken for a free excitation to cross this interaction region. This is due to the long-range characteristics of interactions: as soon as the incoming excitation enters the interaction region, it influences the whole interaction region and the contribution of

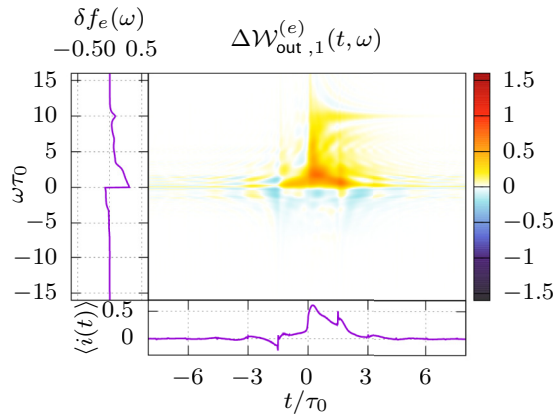


FIG. 16. Wigner function of the outer channel for a Landau excitation with $\omega_0\tau_0 = 10$ going out of a long-range interaction zone in the strong interaction regime ($\theta = \pi/2$), with parameters $l/v_F = 1.5\tau_0$, $\alpha_+ = 1/2$, and $\alpha_- = 1/59$. The finite-frequency admittance of this interaction region has the same low-energy limit than a short-range interaction region with parameters $\tau_+ = \tau_0/2$, $\tau_- = \tau_+/20$. Differences between the long and short-range cases are the apparition of excitations at earlier times, three main peaks in the current instead of two, and a more complex pattern at low energies.

the resulting low-energy electron/hole pairs can be seen near its ends. This means that a first current peak should begin at a time $\tau = l/v_F$ before the arrival of the “real” excitation as can be seen on the figure. Speaking of current, the bottom panel shows that the outgoing current has three main peaks, compared to the two obtained in a short-range setting.

It is then natural to ask whether or not these differences can be detected by an HOM experiment. To answer this question, the top panel of Fig. 17 displays our prediction for both the short and long-range interaction models assuming interaction regions of the same length and the same incoming excitations. As seen from this figure, these two interaction models lead to qualitatively different HOM curves: the long-range one shows a wider dip, as expected of the wider time spreading of the outgoing excitation and more “secondary dips” than the short-range model. This last feature can be traced back to the three main peaks in the outgoing Wigner function computed using the long-range model compared to the two peaks of short-range interactions.

To comment on the experimental state of the art [15,16], the bottom panel of Fig. 17 presents the HOM predictions for parameters corresponding to the recently published experimental results in Ref. [15]. Unfortunately, the side lobes that would enable us to differentiate between the two interaction models occur for a time shift comparable or greater than 300 ps. In practice, probing time shifts larger than 200 ps brings us to values too close to the half-period of the drive which is typically 1 ns. In such situations, it is not possible anymore to forget about the excitation emitted in the other half period: we cannot rely on a single-electron decoherence computation for a quantitative theory/experiment comparison. Probing such large time shifts while comparing to our present theoretical predictions would therefore require lowering the drive frequency f thus deteriorating the signal to noise ratio of the low-frequency current noise measurements.

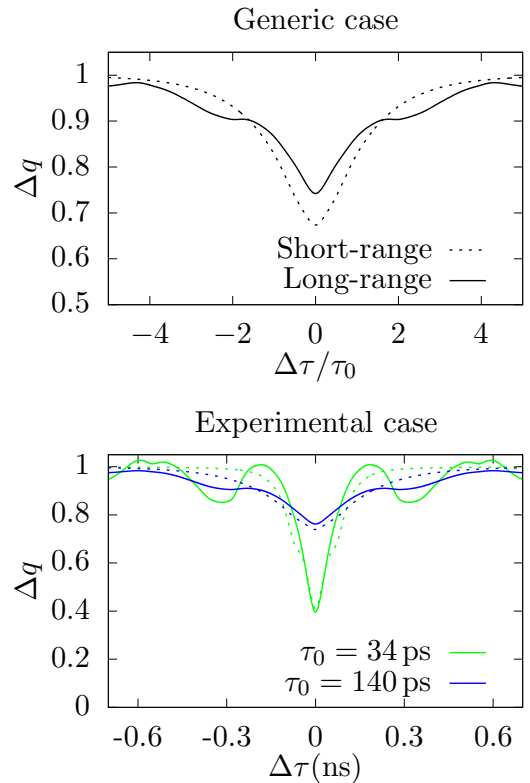


FIG. 17. (Top) Predicted results of an Hong-Ou-Mandel experiment after an interaction region in the short- and long-range cases, at $\nu = 2$. The interaction parameters are the ones given in the caption of Fig. 16 and corresponds to interaction region of the same lengths and with the same low-energy behavior in terms of velocities. The main difference between the predictions of the two models are the depth of HOM dip at $\Delta\tau = 0$ and the secondary dips at $\Delta\tau = \pm 1.5\tau_0$ in the long-range case, which are due to low-energy side excitations seen on Fig. 16. The wider time spreading of the outgoing coherence also leads to a wider HOM dip. (Bottom) Plot of the HOM curves for the long (full lines) and short-range (dotted lines) models with parameters corresponding to the experiment [15].

In our opinion, this calls for complementary investigations and/or experimental developments in order to determine which interaction model for the $\nu = 2$ edge channel system would be the best at reproducing the full HOM curves in detail. By contrast, samples specifically designed for blocking relaxation processes are likely to give much stronger experimental signatures as will be discussed in the forthcoming section.

IV. DECOHERENCE CONTROL

In this section, we consider passive decoherence control by sample design in the $\nu = 2$ edge channel system. The idea is to combine the efficient screening of the edge channel used to propagate the injected electronic excitation to the blocking of energy transfers by closing the other edge channel. In a first experiment [34], electronic relaxation in the outer edge channel has been partially blocked by letting the outer channel propagate along a closed inner edge channel as depicted on Fig. 6(a). In a more recent Mach-Zehnder interferometry

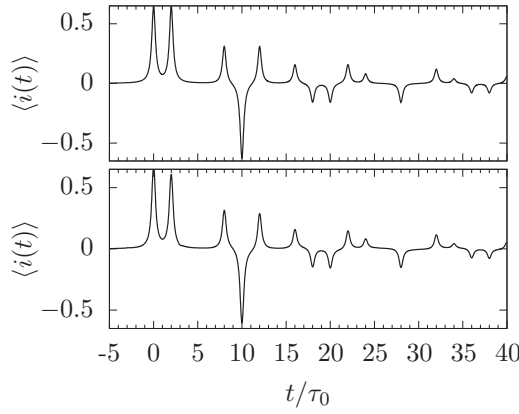


FIG. 18. Outgoing current for an incoming leviton excitation of width $\tau_0/4$ after an interaction with a closed loop. Parameters $\tau_- = \tau_0$, $\tau_+ = 3\tau_0$, and $\tau_L = 7\tau_0$, while not experimentally reasonable, allow a good visualization of the physical properties of this current. The first two peaks corresponding to standard fractionalization when crossing the interaction region are followed by a series of three peaks corresponding to excitations having crossed twice the interaction region and going round the loop once (first corresponds to two crossings in the symmetric mode, then one antisymmetric and one symmetric, third one is two crossings in antisymmetric mode), and so on. (Top) As given by the analytical computation presented in this section. (Bottom) As recovered when integrating the numerically obtained outgoing Wigner function over all energies.

experiment, electronic decoherence has been partially blocked by bordering the propagating edge channel by closed loops [35] as depicted on Fig. 6(b).

We shall now discuss electronic decoherence within both types of samples. We will first discuss what happens to Levitons by looking at edge-magnetoplasmon scattering in the time domain. Understanding this scattering in the frequency domain will then enable us to discuss electronic decoherence of a Landau excitation injected at various energies in Sec. IV B. Finally, a realistic possible sample design for probing the blocking of single-electron decoherence with HOM interferometry will be discussed in Sec. IV C.

A. Magnetoplasmon scattering

1. Time domain

Let us start by analyzing what happens to a percussional voltage pulse $V(t) = V_0\delta(t - t_0)$ sent across the interaction region. The outgoing voltage pulse can be obtained from the inverse Fourier transform of $t(\omega)$ which, using equation (21), can be rewritten as

$$t(\omega) = S_{11}(\omega) \quad (43a)$$

$$+ e^{i\omega\tau_L} S_{12}(\omega) S_{21}(\omega) \sum_{n=0}^{\infty} e^{in\omega\tau_L} S_{22}(\omega)^n. \quad (43b)$$

This expression has a clear physical meaning since all excitations recovered in channel 1 after the interaction region of size l correspond to one of the following paths: term (43a) correspond to incoming excitations directly crossing the region in channel 1, whereas terms (43b) corresponds to

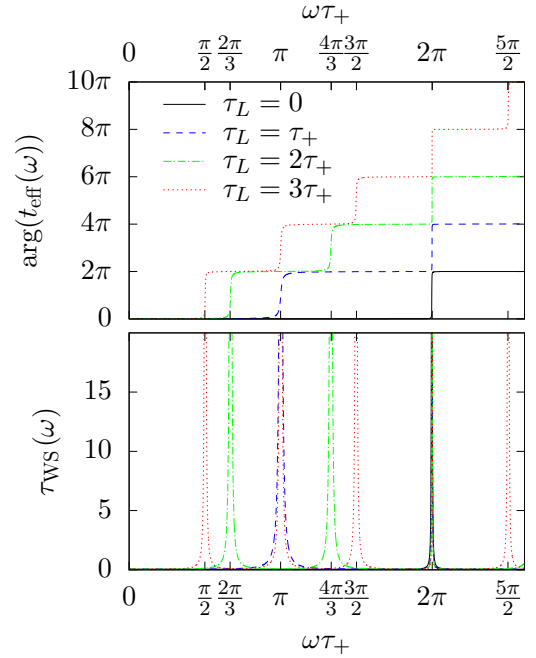


FIG. 19. Phase of the transmission coefficient (top) and the associated dwelling time $\tau_{WS}(\omega)$ (lower) for a short-range interaction with weak coupling ($\theta = \pi/10$) and parameters $\tau_- = \tau_+/20$, for four different geometries for the loop. We see that the phase jumps each time $\omega(\tau_+ + \tau_L) \simeq 2n\pi$, with a stronger jump when $\omega\tau_+ = 2\pi$. These jumps are the signature of a quasibound state (scattering resonance) at corresponding energy inside the loop.

incoming excitations generating excitations in channel 2 (S_{21}), which go round the closed loop and create excitations back in channel 1 (S_{12}). This can either happen after one lap round the loop ($e^{i\omega\tau_L}$) or after $n + 1$ laps, in which case we need to take into account the fact that excitations in channel 2 crossed the interaction region in the second channel n times (S_{22}^n) and made n more laps ($e^{in\omega\tau_L}$).

In the case of short-range interactions, $t(\omega)$ can be rewritten as a sum of complex exponentials:

$$t(\omega) = p_+ e^{i\omega\tau_+} + p_- e^{i\omega\tau_-} + \sum_{n=0}^{\infty} \sum_{k=0}^{n+2} w_{n,k} e^{i\omega((n+1)\tau_L + k\tau_+ + (n+2-k)\tau_-)}, \quad (44)$$

where the weights $w_{n,k}$ are given by²

$$w_{n,k} = q^2 \left[\binom{n}{k} p_+^{n-k} p_-^k + \binom{n}{k-2} p_+^{n+2-k} p_-^{k-2} - 2 \binom{n}{k-1} p_+^{n+1-k} p_-^{k-1} \right]. \quad (45)$$

This equation shows that the outgoing voltage for a localized excitation of charge $-e$ created at time t_0 corresponds to the generation of a percussional current pulse with charge $-ep_+$ emitted at time $t_0 + \tau_+$, another one with charge $-ep_-$ at time

²In this equation, we adopt the convention that $\binom{n}{k} = 0$ if $k > n$ or $k < 0$.

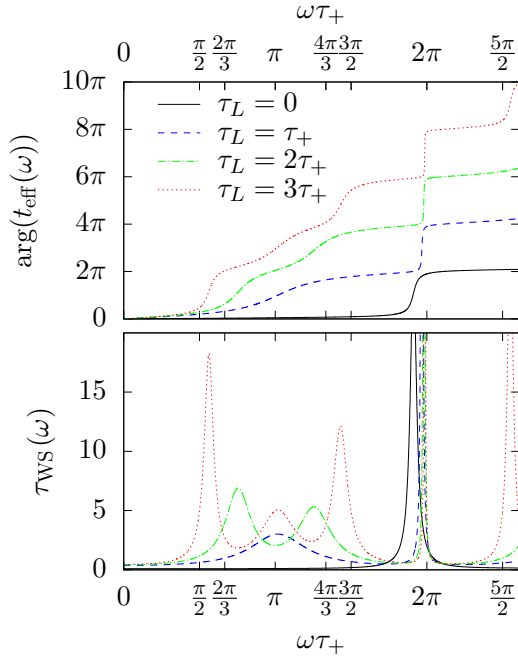


FIG. 20. Phase of the transmission coefficient (top) and associated dwelling time in the closed inner channel (lower) for a short-range interaction with strong coupling ($\theta = \pi/2$) and the same four different geometries for the loop as the low-coupling case. We see that the phase does not go from one plateau to another, but still exhibits jumps at values close to the ones seen before, the jump at $\omega\tau_+ = 2\pi$ being once again the strongest. The corresponding quasibound states inside the loop are therefore broadened in energy.

$t_0 + \tau_-$, and an infinity of others at times $t_0 + (n+1)\tau_L + k\tau_+ + (n+2-k)\tau_-$ with charges $-ew_{n,k}$. The total current is conserved, since $p_+ + p_- = 1$ and $\forall n, \sum_{k=0}^{n+2} w_{n,k} = 0$.

For the Leviton source, with the exact same reasoning, the outgoing state is a sum of time-shifted Leviton excitations with suitable charges. Figure 18 shows the outgoing current for this type of environment computed in two different ways. The top panel of Fig. 18 corresponds to an analytical computation of the expected current in the way we just exposed. The bottom panel is obtained from the numerical computation of the resulting excess Wigner distribution function by integrating over the energy. The very good agreement between the two results illustrates the validity of our numerical approach.

2. Frequency domain

Let us now turn to the transmission coefficient as a function of energy. As stated before, since $|t(\omega)|^2 = 1$, this system behaves as an effective $v = 1$ system but it has a much richer texture than the model presented in Sec. II C 2. First of all, let us consider short-range interactions at weak coupling. The closed inner channel can be seen as a Fabry-Pérot interferometer with low transparency on one side and totally reflecting on the other part. The interaction region can then be viewed as a cavity which is connected to a transmission line. As in optics, the phase of its reflexion coefficient, which is here the edge-magnetoplasmon transmission $t(\omega)$, exhibits sharp resonances. They can arise from quasibound scattering states

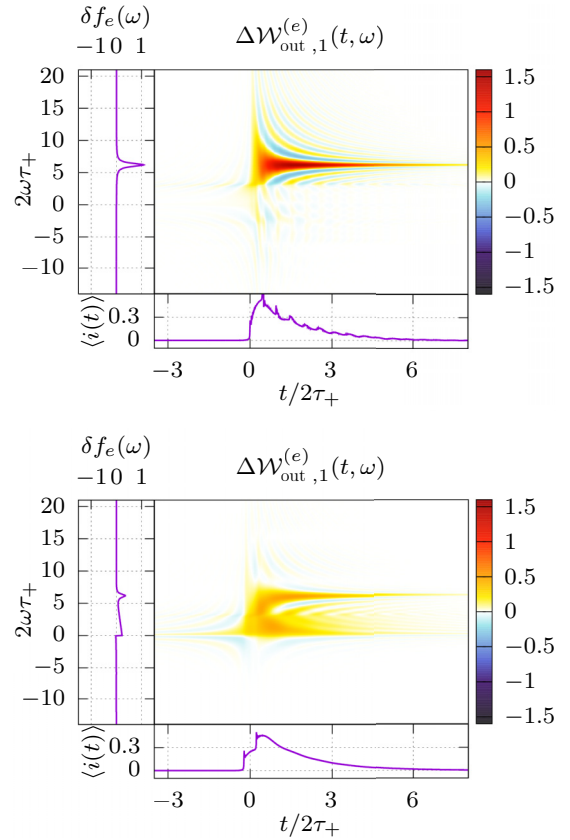


FIG. 21. Outgoing Wigner function for an incoming Landau excitation of duration $\tau_0 = 0.8\tau_+$. Interaction parameters are $\theta = \pi/2$ and $\tau_- = \tau_+/10$. (Top) Short-range interaction with a closed environment of type (a) ($\tau_L = 0$). (Bottom) Co-propagation along an open channel on the same distance with same interaction parameters. For both graphs, the incoming excitation is at an energy $\omega_0\tau_+ = \pi$ below the energy resonances of the loop. When interacting with a closed channel (upper), relaxation is highly suppressed compared to co-propagation along an open channel (lower). Because the injection energy is below closed channel resonances, the outgoing occupation number remains close to the incoming one. Electron/hole pair creation is responsible of the spikes that appear on the average electric current, which are characteristic of the closed channel geometry.

within the interaction region seen as a cavity, which appear as peaks in the Wigner-Smith time delay

$$\tau_{\text{WS}}(\omega) = \frac{1}{2\pi i} \frac{d \ln(t(\omega))}{d\omega}, \quad (46)$$

which represents a dwelling time within the cavity. These resonances are sharply visible in the weak-coupling regime presented on Fig. 19. The top panel depicts the phase of $t_{\text{eff}}(\omega) = e^{-i\omega\tau} t(\omega)$, and displays strong jumps of 2π every time $\omega(\tau_+ + \tau_L) \simeq 2n\pi$. These jumps lead to strong resonances in the Wigner-Smith time delay as seen on the lower panel.

Let us now turn to the strong-coupling case ($\theta = \pi/2$). As is expected from the comparison with a Fabry-Pérot interferometer with higher transparency, the quasibound states inside the loop are broadened in energy, as can be seen on Fig. 20.

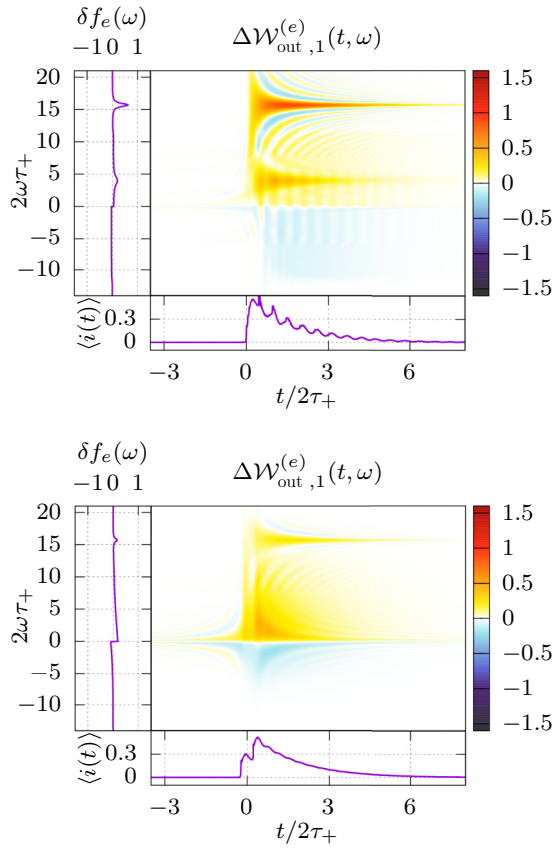


FIG. 22. Same as Fig. 21, but for an incoming excitation above the resonance energy, $\omega_0 \tau_+ = 5\pi/2$. Energy relaxation involves the emission of electron/hole pairs at the resonance energy, leading to a second peak in the energy distribution.

B. Electronic decoherence

We now discuss electronic relaxation and decoherence of Landau excitations at strong coupling in the closed channel geometry depicted on Fig. 6(a) ($\tau_L = 0$). Numerical results for the Wigner function of an electron emitted below the energy of the first resonance of the closed resonator and one emitted between the first and the second resonances are shown on the upper panels of Figs. 21 and 22. These results are compared, on the bottom panel of each figure, to a situation where the interaction region is of the same length but the inner channel is not closed onto itself. The geometry with a closed channel exhibit much less electronic decoherence in comparison with the open channel geometry.

In the first situation depicted in Fig. 21, electron/hole pair generation is inhibited because the electronic energy is off resonance with the cavity and therefore, relaxation is blocked. As a result, no decoherence happens and the excitation leaves the interaction region pretty much unchanged.

When the Landau excitation is injected above the first resonance (see upper panel of Fig. 22), it relaxes by emitting electron/hole pairs precisely at the energy given by the first resonance. This relaxation leads to a peak in the electronic distribution at the final energy of the electron, which is its injection energy minus the resonance energy. The characteristic features of the interaction-generated electron/hole pair

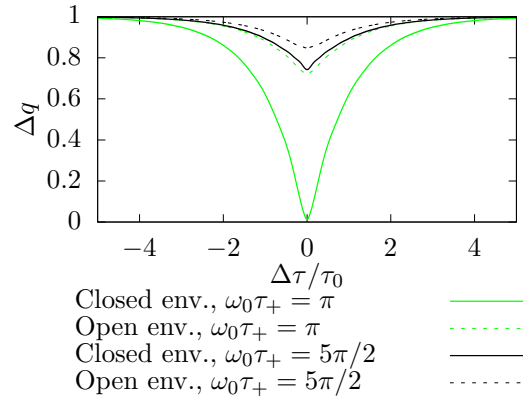


FIG. 23. Results of an Hong-Ou-Mandel experiment for the four Wigner distributions presented in this section. The bigger depth of the HOM dip for the loop environment proves that closing the environment on itself provides a net advantage compared to the open case. Specifically, in the case where the excitation is emitted below the first level in the loop ($\omega \tau_+ = \pi$), we see a dip going nearly all the way down to 0, which denotes a quasicomplete protection from decoherence.

cloud are the temporal oscillations of $\Delta \mathcal{W}^{(e)}(t, \omega)$ for ω below the peak associated with the relaxed electron. HOM interferometry can then be used to check whether or not we are protected against decoherence. As shown on Fig. 23, the HOM dip for wave packets propagating along a closed inner channel should be bigger than their opened counterpart, going even down close to zero for an excitation emitted below the first resonance.

C. A realistic sample proposal

In this section, we discuss a possible geometry in which Landau excitations such as the one emitted by the mesoscopic capacitor [20] would be protected against decoherence. One may naively think that loops smaller than the size of dots used to emit the excitation would be needed, which seems unreasonable experimentally. Luckily, previous experimental studies [86] have shown that the speed of electronic excitations in top-gated regions of the 2DEG are smaller than the “free” velocity, a fact that can be checked using available experimental data on the energies of the quantum dot. The energy $\hbar\omega_0$ of Landau particles emitted by the dot used in Ref. [15] is around $60 \mu\text{eV}$, the size of the dot being $2 \mu\text{m}$, leading to a relevant velocity in gated region of the 2DEG $v^{\text{gate}} \sim 5.8 \times 10^4 \text{ m s}^{-1}$. The dwelling time of excitations in the dot is $\tau_0 \simeq 100 \text{ ps}$, leading to a typical width in energy of about 1/10th of the injection energy. Consequently, a safe limit for blocking decoherence would be to have a loop such that $\omega_0(\tau_+ + \tau_L) < 3\pi/2$. The edge-magnetoplasmon modes populated within the incoming electronic excitations have their energies below the resonance, even when considering the resonance width.

A sample design with a loop of total size $4 \mu\text{m}$ is sketched on Fig. 24. We predict protection against decoherence for the single-electron excitations we are interested in. Of course, by tuning the dot parameters for emitting excitations at lower energies, decoherence protection would still be

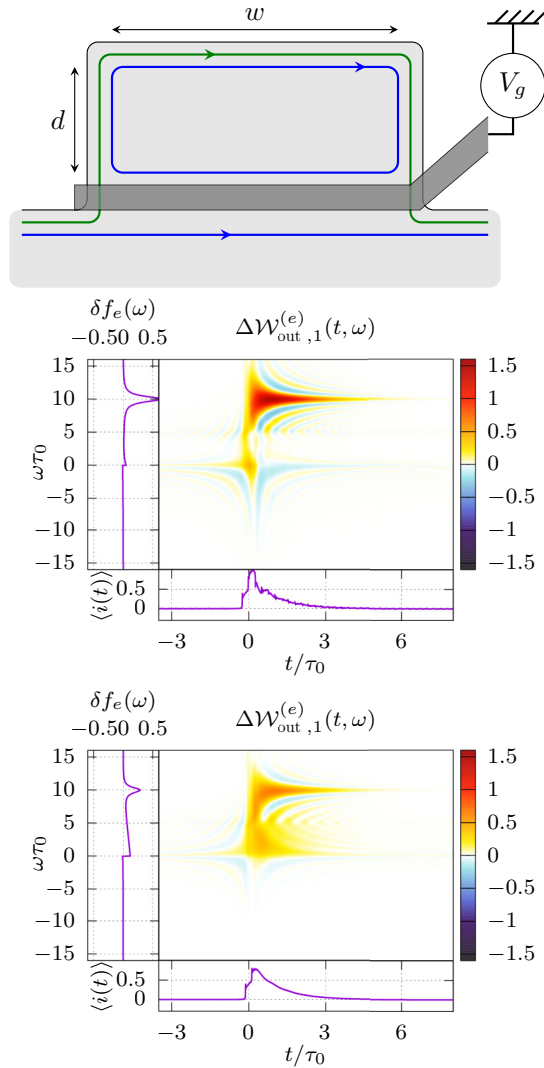


FIG. 24. (Top) Possible experimental design for testing decoherence control on a Landau excitation. Here, the 2DEG (in light gray) defines a cavity delimited by a top gate shifting the electron density so that only the outer edge channel can pass through. This creates a region with a closed inner channel. The single-electron source as well as the QPC of the HOM probe should be located close to the loop. The loop corresponds to $\tau_+ = (w + 2d)/v_+^{\text{chem.}}$ and $\tau_L = w/v_F^{\text{gate}}$, where $v_+^{\text{chem.}}$ denotes the speed of the slow mode in chemically defined edge channels, whereas v_F^{gate} is the Fermi velocity in an edge channel propagating along a metallic gate. (Middle) Outgoing Wigner function when $w = 1.5 \mu\text{m}$, $h = 0.5 \mu\text{m}$ for an incoming excitation with parameters $\omega_0\tau_0 = 10$ and $\tau_0 = 100 \text{ ps}$. The velocities are $v_+^{\text{chem.}} = 1 \times 10^5 \text{ m s}^{-1}$ and $v_F^{\text{gate}} = 5.8 \times 10^4 \text{ m s}^{-1}$. (Bottom) Wigner function in the case where the gate closing the loop is used to either let both channels through or none (times of flight are equivalent in those two cases). Decoherence would be far more important in such cases where the inner channel is not closed on itself.

possible even with two times larger loops (see Appendix G, Fig. 27). The design presented here would allow a test of decoherence protection for single-electron excitations emitted by the mesoscopic capacitor driven by square pulses. Electronic decoherence and relaxation of energy resolved

single-electron excitations being stronger than for an out of equilibrium distribution generated by a biased QPC, such an experiment would provide a stronger test of the potential of sample design for decoherence protection.

Finally, as was presented on Fig. 22, larger loops with $2\pi \leq \omega_0(\tau_+ + \tau_L) \leq 4\pi$ give access to the physics of electronic excitations accompanied by a single plasmon around an energy given by the first scattering resonance of the loop. This allows the probing of new hybrid quantum single-electron and single-plasmon excitations and calls for new measurement protocols to fully characterize these excitations.

V. CONCLUSION AND PERSPECTIVES

To conclude, we have addressed the question of decoherence control for single-electron excitation propagating within chiral edge channels through the properties of the material itself and sample design. Using a semirealistic model for long-range interactions within a single ideal chiral channel, we have found that a high bare Fermi velocity may be significantly more promising for limiting decoherence for two reasons: first, it leads to a lower effective QED coupling constant, a point that has indeed been overlooked, and next it amplifies the distance covered within a given time of flight. The conjugation of these two effects could lead to a drastic decrease of electronic decoherence over distances of 10 to 100 μm as long as dissipative effects could be neglected. We think that this calls for more thorough experimental studies to explore the potential of different materials for electron quantum optics. Moreover, our analysis once again stresses the importance of performing electronic decoherence experiments in setups where finite-frequency ac transport could also be measured.

We have also shown that passive decoherence protection through sample design could be tested for excitations emitted by the mesoscopic capacitor in the single-electron regime using, for example, an HOM experiment. We have proposed a realistic design for demonstrating this effect. Moreover, our study suggests that such samples could be used for emitting single edge magnetoplasmons thus opening the way to hybrid electron-and-photon quantum optics.

These predictions being obtained within the framework of bosonization that assumes as a starting point a linear spectrum for bare fermions, it is natural to ask how our results are affected when the nonlinearity of the electron's dispersion relation cannot be neglected. This is not a purely theoretical question since experiments [24,87] performing single-electron injection at much higher energies than the mesoscopic capacitor are certainly beyond the validity range of our computations. Motivated by cold atom experiments, 1D quantum wires and 1D quantum spins systems, a considerable amount of work, extensively reviewed by Imambekov *et al.* [88], has been devoted to explore 1D quantum fermionic liquids beyond the Luttinger liquid paradigm. As pointed out by these authors, attempts at treating electronic dispersion perturbatively within the standard bosonization framework are doomed by the strong degeneracy of the original bosonic spectrum.

A recently developed alternative bosonization scheme [89] offers interesting perspective to extend our work to this case. In this formalism, the dictionary between localized electronic excitations and bosonic modes is still relatively simple but the

relation between charge density and bosonic modes is no more linear. Consequently, the main challenge would be to deal with a nonquadratic Hamiltonian within the interaction region but there might be interaction regimes in which the effect of interactions could be approximately described by an elastic scattering with a reasonable accuracy. Although very challenging, this is certainly a line of research worth exploring.

More generally, investigating electronic decoherence induced by other systems than a standard harmonic environmental channels with regular spectral functions at low energy is important for future experimental developments. As a first example, understanding the effect of a highly nonlinear system such as a double dot capacitively coupled to an edge channel on single to few electron excitations is certainly an interesting perspective. It would open the way for probing the correlated states of electrons close a quantum impurity (Kondo cloud) using electronic excitations. Coherent transport of levitons through a Kondo impurity has been recently studied using perturbative electronic diagrammatics [90], a framework that captures the low-temperature Fermi-liquid behavior. However, it would be interesting to analyze beyond this regime and in a more general way what insight can be obtained from probing quantum impurities and their surroundings using electron quantum optics sources. Beyond electron quantum optics, investigating this problem is certainly relevant for microwave quantum optics since suitable circuit QED systems simulate the spin boson problem [91] and, as a long term perspective, for Kondo systems simulated by alkaline-earth atoms in an optical lattice [92], a platform that might give access to the real time formation and evolution of the Kondo cloud.

Another relevant question is the effect of the ubiquitous $1/f$ noise present in solid state devices [93]. Such a noise could effectively be generated by a suitable distributions of weakly coupled two level systems. It has been proposed that $1/f$ noise could lead to strong renormalization in tunneling experiments performed on quantum Hall edge channels, leading to a change of exponents in dc tunneling experiments [94]. As of now, low frequency noise has been shown to be negligible in experiments [96] above 20 KHz, much lower than any of the typical frequency scales associated with the time scales involved in the experiment (typically, close to or above the GHz). Moreover, its amplitude is small enough to view it as a slowly varying classical noise on the reference chemical potential whose amplitude should not alter our conclusions. Nevertheless, it would be interesting to study the effect of a harmonic environment with a much stronger $1/f$ spectral density on electronic decoherence in the spirit of Ref. [95].

ACKNOWLEDGMENTS

We thank C. Bauerle, J.M. Berroir, E. Bocquillon, V. Freulon, F.D. Parmentier, P. Roche, B. Plaças and X. Waintal for useful discussions. This work is supported by the ANR grant “Ishot reloaded” (ANR-14-CE32-0017) and ERC Consolidator grant “EQUO” (No. 648236).

APPENDIX A: BOSONIZATION

Bosonization provides a description of a 1D chiral relativistic gas of fermions in terms of bosonic degrees of freedom

corresponding to charge density waves [75]. It has been extensively used to describe quantum systems in one dimension [74] such as the nonchiral Luttinger liquid [11] and quantum Hall edge channels [56].

In the present case of a 1D chiral relativistic channel at a given chemical potential μ , the excess charge density $n(x, t)$ is the normal ordered product $:(\psi^\dagger\psi): (x)$ with respect to the corresponding Fermi energy. It is expressed in terms of a quantum bosonic field ϕ

$$:(\psi^\dagger\psi): (x, t) = \frac{1}{\sqrt{\pi}} (\partial_x\phi)(x, t) \quad (\text{A1})$$

whose mode decomposition can be written in terms of creation $b^\dagger(\omega)$ and destruction operators $b(\omega)$ called edge-magnetoplasmon modes:

$$\phi(x, t) = \frac{-i}{\sqrt{4\pi}} \int_0^{+\infty} (b(\omega)e^{i\omega(x/v_F-t)} - \text{H.c.}) \frac{d\omega}{\sqrt{\omega}}, \quad (\text{A2})$$

where v_F denotes the Fermi velocity of fermionic excitations in this chiral channel. The edge-magnetoplasmon modes can be expressed in terms of the fermionic mode operators $c(\omega)$ and $c^\dagger(\omega)$ defined by

$$\psi(x, t) = \int_{-\infty}^{+\infty} c(\omega) e^{i\omega(x/v_F-t)} \frac{d\omega}{\sqrt{2\pi v_F}} \quad (\text{A3})$$

through

$$b^\dagger(\omega) = \frac{1}{\sqrt{\omega}} \int_{-\infty}^{+\infty} c^\dagger(\omega + \omega')c(\omega') d\omega'. \quad (\text{A4})$$

This immediately shows that $b^\dagger(\omega)$ creates a coherent superposition of electron/hole pairs with energy $\hbar\omega$. Using Eq. (9), the finite-frequency modes of the excess electronic current $i(x, t) = -ev_F n(x, t)$ are directly proportional to the edge-magnetoplasmon modes, $i(\omega > 0) = -e\sqrt{\omega}b(\omega)$. The electronic operator can be expressed in terms of these bosonic modes through

$$\psi(x, t) = \frac{\mathcal{U}}{\sqrt{2\pi a}} \exp(i\sqrt{4\pi}\phi(x, t)), \quad (\text{A5})$$

where a is an ultraviolet cutoff that gives the length scale below which bosonization is not valid and \mathcal{U} (respectively, \mathcal{U}^\dagger) is the ladder operator suppressing (respectively, adding) one electron from the reference vacuum.

The fermionic operator $\psi^\dagger(x, t)$ thus performs two things: it shifts the vacuum state to add one electronic charge $-e$ to it and then it acts as a displacement operator on the edge-magnetoplasmon modes with parameter $\Lambda_\omega(x, t) = e^{-i\omega(x/v_F-t)}/\sqrt{\omega}$:

$$D[\Lambda(x, t)] = \exp\left(\int_0^{+\infty} (\Lambda_\omega(x, t)b^\dagger(\omega) - \text{H.c.})d\omega\right). \quad (\text{A6})$$

As discussed in Ref. [68], a classical time-dependent voltage drive $V(t)$ generates an edge-magnetoplasmon coherent state with parameter $\Lambda_\omega[V(t)] = -e\tilde{V}(\omega)/h\sqrt{\omega}$. The coherent state of parameter $\Lambda_\omega(x, t)$ thus corresponds to the single-electron state generated by a voltage pulse $V(t) = -(h/e)\delta(t - x/v_F)$ generating a percussional current pulse carrying a single-electron charge.

APPENDIX B: A LONG-RANGE MODEL FOR $\nu = 1$

In this section, we derive an exact expression for the edge-magnetoplasmon transmission coefficient in the $\nu = 1$ case using a simple model of Coulomb interaction based on discrete elements in the spirit of Büttiker's treatment of high-frequency quantum transport [72]. Electrons within the interaction region see the electric potential $U(x, t)$ given by a capacitive coupling inside a finite length region of size l :

$$U(x, t) = \begin{cases} 0 & \text{if } x \notin \left[-\frac{l}{2}, \frac{l}{2}\right] \\ \frac{1}{C} \int_{-\frac{l}{2}}^{\frac{l}{2}} n(y, t) dy & \text{otherwise} \end{cases}, \quad (\text{B1})$$

where the excess density of charges n is itself linked to the bosonic field ϕ through equation (9). Equation (10) can be recast as a closed equation on ϕ expressed in the frequency domain as

$$(-i\omega + v_F \partial_x) \phi(x, \omega) = \frac{e^2}{hC} \left(\phi\left(-\frac{l}{2}, \omega\right) - \phi\left(\frac{l}{2}, \omega\right) \right). \quad (\text{B2})$$

Expressing $\phi(x, \omega)$ as $e^{i\omega x/v_F} \varphi_\omega(x)$ leads to

$$\begin{aligned} \partial_x \varphi_\omega(x) &= \frac{e^2}{v_F h C} e^{-i\omega x/v_F} \\ &\times \left(e^{-i\omega l/(2v_F)} \varphi_\omega\left(-\frac{l}{2}\right) - e^{i\omega l/(2v_F)} \varphi_\omega\left(\frac{l}{2}\right) \right), \end{aligned} \quad (\text{B3})$$

which can be integrated over the whole interaction region to give us a relation between $\varphi_\omega(-\frac{l}{2})$ and $\varphi_\omega(\frac{l}{2})$. Finally, the solution reads

$$\phi\left(\frac{l}{2}, \omega\right) = t(\omega) \phi\left(-\frac{l}{2}, \omega\right), \quad (\text{B4})$$

where

$$t(\omega) = e^{i\omega l/v_F} \frac{1 + A(\omega, l) e^{-i\omega l/(2v_F)}}{1 + A(\omega, l) e^{i\omega l/(2v_F)}}, \quad (\text{B5a})$$

$$A(\omega, l) = \frac{4e^2/C}{h v_F/l} \text{sinc}\left(\frac{\omega l}{2v_F}\right), \quad (\text{B5b})$$

in which we recognize the kinetic energy scale $h v_F/l$ as well as the dimensionless ratio $\alpha = e^2 l / C h v_F$ of the electrostatic energy e^2/C to this kinetic energy scale, which quantifies the strength of Coulomb interactions in this system. Note that, at least for sufficiently long edge channels, this coupling constant does not depend on the length l since C also scales as l .

As expected, the transmission coefficient $t(\omega)$ is of modulus 1 because no energy can be lost in a $\nu = 1$ setup without any dynamical environment. The quantity of interest is therefore the phase of $t(\omega)$.

In the limit where Coulomb interaction effects can be neglected ($\alpha \rightarrow 0$), $t(\omega) = e^{i\omega l/v_F}$ showing that the bare Fermi velocity is recovered. The opposite limit of ultrastrong Coulomb interactions ($\alpha \rightarrow \infty$) leads to $t(\omega) = 1$, that is, an infinite edge-magnetoplasmon velocity. However, at fixed coupling α , the edge-magnetoplasmon velocity tends to $v_\infty = v_F$ when $\omega l/v_F \gg 1$. At low frequency, we find that the

time of flight of edge magnetoplasmons is renormalized thus leading to an increased renormalized plasmon velocity

$$\frac{v_0}{v_\infty} = 1 + \frac{4e^2/C}{h v_\infty/l} \quad (\text{B6})$$

compared to the velocity at high frequency, which is the bare Fermi velocity v_F .

To estimate an order of magnitude of this ratio, let us remind that C being the capacitance of the interaction region that is roughly similar to a 1D wire, $C \simeq 2\pi \epsilon_0 \epsilon_r l$ up to a geometrical factor for large l , that is when boundary effects are small. Consequently, α does not depend on l but behaves as [68]

$$\alpha \simeq \frac{\alpha_{\text{qed}}}{\pi \epsilon_r} \times \frac{c}{v_F} \times (\text{geometrical factor}), \quad (\text{B7})$$

where α_{qed} denotes the fine-structure constant, ϵ_r the relative permittivity of the material and v_F the bare Fermi velocity.

For AlGaAs/GaAs, one usually estimates $v_F \simeq 10^5$ m/s and $\epsilon_r \simeq 10$ thus leading to

$$\alpha \simeq 0.75 \times (\text{geometrical factor}). \quad (\text{B8})$$

Assuming a geometrical factor of order 1, this gives a velocity for low-energy magnetoplasmons of the order of $v_0 \sim 4 \times 10^5$ m/s, which is compatible to what is observed in $\nu = 2$ edge channel systems [97]. Let us remind that the edge-magnetoplasmon velocity depends on the details of the electric potential seen by electrons near the edge of the 2DEG and therefore of the conception of the sample. This is precisely used in the above reference to modulate it by polarising gates.

In the case of graphene, a common estimation for the Fermi velocity is of the order of $v_F \simeq 1 \times 10^6$ m/s and $\epsilon_r \simeq 14$ [69,98] thus leading to

$$\alpha \simeq 0.054 \quad (\text{B9})$$

when using a geometrical factor equal to unity. The coupling constant is much lower and therefore $v_0/v_F \simeq 1.2$. Let us stress that, as far as we know, no direct measurement of v_F in quantum Hall edge channels of graphene have been performed but if this commonly discussed value is confirmed, this would put graphene in a totally different coupling range than AlGaAs/GaAs.

For intermediate values of the coupling constant α , as shown on Fig. 5, the edge-magnetoplasmon velocity deduced from $t(\omega)$ presents a decay from v_0 to a regime with small oscillations above the asymptotic value of v_F .

Expanding the phase of $t(\omega)$ in powers of $\omega \tau_0$ leads to

$$\begin{aligned} \phi(\omega) &= \omega \tau_0 + \frac{\alpha}{3} (\omega \tau_0)^3 + \frac{8\alpha}{90} (\alpha^2 + 2\alpha - 1/8) (\omega \tau_0)^5 \\ &+ \mathcal{O}((\omega \tau_0)^7), \end{aligned} \quad (\text{B10})$$

which, as explained Appendix F, gives us the low-energy expansion of the inelastic scattering probability.

APPENDIX C: DISCRETE ELEMENT CIRCUIT DESCRIPTION

In this appendix, we discuss the circuit synthesis for the edge-magnetoplasmon transmission amplitude in the case of

an ideal $\nu = 1$ edge channel and we obtain its first non trivial Caer form. We then connect the discrete circuit element parameters to the parameters of the model presented in Appendix B.

1. Circuit synthesis for an ideal $\nu = 1$ edge channel

Using the relation $t(\omega) = 1 - R_K G(\omega)$ where $G(\omega)$ is the finite-frequency admittance of the discrete element circuit of Fig. 7, the transmission amplitude $t(\omega)$ can be expressed in terms of the impedance $Z(\omega)$ as

$$t(\omega) = \frac{1 + \omega C_\mu \Im(Z(\omega)) + i\omega C_\mu [R_K - \Re(Z(\omega))]}{1 + \omega C_\mu \Im(Z(\omega)) - i\omega C_\mu \Re(Z(\omega))}. \quad (\text{C1})$$

Consequently, $t(\omega)$ is a pure phase if and only if $\Re(Z(\omega)) = R_K/2$ at all frequencies. We can then write

$$t(\omega) = \frac{1 + i\beta(\omega)}{1 - i\beta(\omega)} = \exp[2i \arctan(\beta(\omega))], \quad (\text{C2})$$

where

$$\beta(\omega) = \frac{\omega R_K C_\mu}{2} \frac{1}{1 + \omega C_\mu \Im(Z(\omega))}. \quad (\text{C3})$$

With our conventions, the reactance $\Im(Z(\omega))$ is a strictly decreasing function of ω [99]. Since, by definition, the electrochemical capacitance C_μ contains the low-frequency divergence of the ZC circuit, it is expected to be regular at low frequency, starting with a zero at $\omega = 0$ and then alternating poles and zeros. A suitable low-frequency expansion of $t(\omega)$ can then be obtained using a Caer form of circuit synthesis which leads to a continuous fraction expansion of the finite-frequency admittance.

The simplest case corresponds to the circuit depicted on the right panel of Fig. 7. It leads to

$$\beta(\omega) = \frac{\omega R_K C_\mu}{2} \frac{1 - \omega^2 LC}{1 - \omega^2 L(C + C_\mu)}. \quad (\text{C4})$$

Expanding $2 \arctan(\beta(\omega))$ in powers of $\omega R_K C_\mu$ then leads to the low-frequency finite-frequency admittance up to order $(\omega R_K C_\mu)^6$:

$$g(\omega) = -i\omega R_K C_\mu + \frac{1}{2}(\omega R_K C_\mu)^2 \quad (\text{C5a})$$

$$-i \left[\frac{L/R_K}{R_K C_\mu} - \frac{1}{4} \right] (\omega R_K C_\mu)^3 \quad (\text{C5b})$$

$$+ \left[\frac{L/R_K}{R_K C_\mu} - \frac{1}{8} \right] (\omega R_K C_\mu)^4 \quad (\text{C5c})$$

$$-i \left[\left(1 + \frac{C}{C_\mu} \right) \left[\frac{L/R_K}{R_K C_\mu} \right]^2 + \frac{1}{16} - \frac{3}{4} \frac{L/R_K}{R_K C_\mu} \right] \times (\omega R_K C_\mu)^5, \quad (\text{C5d})$$

which then leads to Eq. (F2).

Being described by two parameters (L and C) besides C_μ and $R_q = R_K/2$, this circuit provides an expansion of $\phi(\omega)$ up to order $(\omega R_K C_\mu)^5$. In order to capture the low-frequency behavior of $\phi(\omega)$ to the next non trivial orders (7 and 9), we need to go one step further in the Caer form of the circuit. This would correspond to adding another LC impedance in

series with the capacitor C . This process can then be iterated to reconstruct the full ω dependence of $\Im(Z(\omega))$.

2. Extracting the discrete element parameters

Let us now derive the discrete element circuit parameters for the interaction model at $\nu = 1$ considered in Appendix B. Expanding the admittance at low frequency and identifying this expansion with (C5) leads to

$$R_K C_\mu = \tau_0 = l/v_0, \quad (\text{C6a})$$

$$\frac{L/R_K}{R_K C_\mu} = \frac{1 + 4\alpha}{12}, \quad (\text{C6b})$$

$$\frac{C}{C_\mu} = \frac{1 + 4\alpha}{5}. \quad (\text{C6c})$$

The inductance L as well as the capacitance C increase when increasing the effective Coulomb interaction strength. This is expected since increasing Coulomb interactions tend to increase the velocity ratio v_0/v_∞ . In this model the ratio of L/C to R_K^2 remains constant and equal to $5/12$.

APPENDIX D: PHENOMENOLOGICAL MODELS FOR PLASMON VELOCITY

Let us discuss problems that arise for some phenomenological expressions for the edge magnetoplasmons in the ideal $\nu = 1$ case. We first consider the phenomenological expression

$$\frac{v(\omega)}{v_0} = \frac{1 + \frac{v_\infty}{v_0} (\omega/\omega_c)^2}{1 + (\omega/\omega_c)^2}, \quad (\text{D1})$$

which interpolates between v_0 at low frequency and v_∞ at high frequency, the crossover scale being ω_c . We shall denote by $\tau_0 = l/v_0$. The finite-frequency admittance only depends on the dimensionless variable $\omega\tau_0$ and parameters $0 < v_\infty/v_0 \leq 1$ and $\omega_c\tau_0 > 0$. Compared to the long-range interaction model detailed in Appendix B, this phenomenological expression avoids oscillations in the edge-magnetoplasmon velocity and it depends on one more parameter than just l/v_0 and the coupling constant. However, as we will see now, is it not physically acceptable!

A first hint of a problem comes from the low-energy expansion using a discrete element circuit description that reproduces the same $t(\omega)$ dependence up to order 5. Then, under this condition, the electrochemical capacitance C_μ , the inductance L and the capacitance C of the first ladder in the Caer expansion are given by

$$R_K C_\mu = \tau_0, \quad (\text{D2a})$$

$$\frac{L/R_K}{R_K C_\mu} = \frac{1}{12} + \left(1 - \frac{v_\infty}{v_0} \right) \frac{1}{(\omega_c\tau_0)^2}, \quad (\text{D2b})$$

$$\frac{C}{C_\mu} = \frac{\frac{1}{720} + \left(1 - \frac{v_\infty}{v_0} \right) \left[\frac{1}{60(\omega_c\tau_0)^2} - \frac{1}{(\omega_c\tau_0)^4} \right]}{\left(\frac{1 - v_\infty/v_0}{(\omega_c\tau_0)^2} + \frac{1}{12} \right)^2}. \quad (\text{D2c})$$

As expected, the eigenfrequency $1/\sqrt{LC\mu}$ corresponds, up to renormalization, to ω_c . Since $v_\infty \leq v_0$ these expressions

give a physical value for the inductance L but C/C_μ sometimes becomes negative! This is a serious hint that Eq. (D1) is not a physically meaningful ω -dependence for the edge-magnetoplasmon velocity. This can be seen by considering the analytical continuation of $\Re(1 - t(\omega))$ to the complex plane $s = \sigma + i\omega$, which must be positive for $\sigma < 0$: it exhibits singularities (and thus negativities) on the negative real axis ($\sigma < 0$ and $\omega = 0$).

In the same way, a phenomenological edge-magnetoplasmon velocity with a sharper high-energy stabilization towards v_∞ such as [100,101]

$$\frac{v(\omega)}{v_\infty} = 1 + \frac{v_0 - v_\infty}{v_\infty} e^{-(\omega\tau_e)^2} \quad (\text{D3})$$

is not physical within our framework because the analytical continuation of $\Re(1 - e^{i\omega l/v(\omega)})$ also presents singularities in the half plane $\sigma + i\omega$ for $\sigma < 0$.

APPENDIX E: HIGH-ENERGY DECOHERENCE AND RELAXATION

1. General results

For a single-electron excitation injected at high energy, the contribution to electronic coherence $\varphi_e(t) \varphi_e^*(t')$ picks up an effective decoherence coefficient $\mathcal{D}(t - t')$ so that [32]

$$\Delta \mathcal{G}_{\text{WP}}^{(e)}(t|t') \simeq \varphi_e(t) \varphi_e^*(t') \mathcal{D}(t - t'), \quad (\text{E1})$$

which, at $\nu = 1$, is equal to the overlap $\langle g(t')|g(t) \rangle$ of the electron/hole pair clouds generated by Coulomb interactions:

$$\mathcal{D}(\tau) = \exp\left(\int_0^{+\infty} |1 - \tilde{\tau}(\omega)|^2 (e^{i\omega\tau} - 1) \frac{d\omega}{\omega}\right). \quad (\text{E2})$$

an expression analogous to the one appearing in the weak-coupling description of dynamical Coulomb blockade across a tunnel junction [102]. The relaxation kernel

$$\tilde{\mathcal{D}}(\omega') = \int_{-\infty}^{+\infty} e^{-i\omega'\tau} \mathcal{D}(\tau) d\tau. \quad (\text{E3})$$

can then be decomposed into an elastic and an inelastic part: $\tilde{\mathcal{D}}(\omega') = 2\pi(Z_\infty \delta(\omega') + d(\omega'))$, where

$$Z_\infty = \exp\left(-\int_0^{+\infty} |1 - \tilde{\tau}(\omega)|^2 \frac{d\omega}{\omega}\right) \quad (\text{E4})$$

is nothing but the high-energy limit of the elastic scattering probability $|\mathcal{Z}(\omega)|^2$. The inelastic part $d(\omega)$ describes electronic relaxation: it represents the probability that the electron has lost energy ω . It is determined by the integral equation

$$\omega d(\omega) = |1 - \tilde{\tau}(\omega)|^2 + \int_0^\omega |1 - \tilde{\tau}(\omega')|^2 d(\omega - \omega') d\omega', \quad (\text{E5a})$$

which can readily be solved on a computer using the initial condition that $d(\omega \rightarrow 0^+) \rightarrow \lim_{\omega \rightarrow 0^+} (|1 - \tilde{\tau}(\omega)|^2/\omega)$. It can also be expressed as a formal series corresponding to the various processes involving the emission of an increasing number of pairs of electron/hole excitations, exactly the same structure than in the dynamical Coulomb blockade theory [102]. With these notations, the elastic part of the outgoing

Wigner function is well separated from the inelastic part:

$$\Delta \mathcal{W}_{\text{WP}}^{(e)}(t, \omega) = Z_\infty \mathcal{W}_{\varphi_e}(t, \omega) \quad (\text{E6a})$$

$$+ \int_0^\omega d(\omega') \mathcal{W}_{\varphi_e}(t, \omega + \omega') d\omega', \quad (\text{E6b})$$

where $\mathcal{W}_{\varphi_e}(t, \omega)$ denotes the Wigner function associated to the incoming wave packet φ_e .

2. Energy dissipation at $\nu = 1$

Let us discuss energy dissipation through the creation of electron/hole pairs in the $\nu = 1$ ideal edge channel in the regime discussed above. We shall thus assume that the spectral weight of the incoming electron as well as of the contribution $\mathcal{G}_{\text{WP},1}^{(e)}$ to the outgoing coherence are well above the vicinity of the Fermi level.

The incoming average energy comes from the injected electron and is equal to

$$E_{\text{in}} = \hbar \int_0^{+\infty} |\tilde{\varphi}_e(\omega)|^2 \omega \frac{d\omega}{2\pi v_F}, \quad (\text{E7})$$

using the convention

$$\tilde{\varphi}_e(\omega) = v_F \int_{-\infty}^{+\infty} \varphi_e(-v_F t) e^{i\omega t} dt \quad (\text{E8})$$

for defining the electronic wave packet in the frequency domain from the original wavefunction φ_e in the spatial domain.

The outgoing average energy then consists of two parts: the energy carried by the injected electron which has flown across the interaction region either elastically or inelastically, and the energy of electron/hole excitations created by its passing through. The first contribution is

$$E_{\text{out}}^{(e)} = Z_\infty E_{\text{in}} \quad (\text{E9a})$$

$$+ \hbar \int_{(\mathbb{R}^+)^2} |\varphi_e(\omega)|^2 (\omega - \omega') d(\omega') d\omega' \frac{d\omega}{2\pi v_F}. \quad (\text{E9b})$$

The first line corresponds to elastic scattering and the second line to inelastic processes in which the electron has fallen down from $\hbar\omega$ to $\hbar(\omega - \omega')$. There, the integrals are extended to $+\infty$ safely because of our working hypothesis: the relaxation tail is well above the Fermi level. We then use that $\int_0^{+\infty} d(\omega') d\omega' = 1 - Z_\infty$ and the normalization condition of the wave packet to rewrite this as

$$E_{\text{out}}^{(e)} = E_{\text{in}} - \hbar \int_0^{+\infty} \omega' d(\omega') d\omega'. \quad (\text{E10})$$

Energy conservation, which is true on average, shows that the dissipated energy in electron/hole pair creation is equal to

$$E_{\text{out}}^{(\text{diss})} = \hbar \int_0^{+\infty} \omega d(\omega) d\omega. \quad (\text{E11})$$

Recognizing that $\int_0^{+\infty} \omega d(\omega) d\omega$ corresponds to the derivative of the decoherence coefficient $\mathcal{D}(\tau)$ when $\tau \rightarrow 0^+$ leads to

$$E_{\text{out}}^{(\text{diss})} = \hbar \int_0^{+\infty} |1 - \tilde{\tau}(\omega)|^2 d\omega. \quad (\text{E12})$$

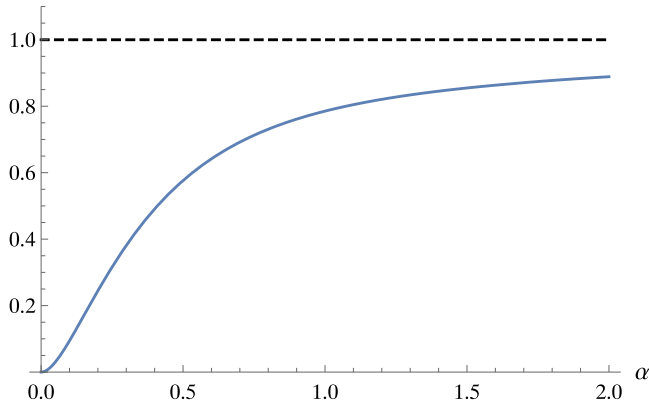


FIG. 25. Dependence on the coupling constant α of $E_{\text{out}}^{(\text{diss})}(\alpha, hv_F/l)$ in units of hv_0/l , where $E_{\text{out}}^{(\text{diss})}(\alpha, hv_F/l)$ denotes the average energy dissipated by a hot electron given by Eq. (E13) corresponding to the model discussed in Appendix B.

Using the transmission coefficient given by Eq. (B5), the dissipated energy is given by

$$E_{\text{out}}^{(\text{diss})} = \frac{hv_F}{\pi l} \int_0^{+\infty} \frac{64\alpha^2 \sin^4(u) du}{(u + 2\alpha \sin(2u))^2 + 16\alpha^2 \sin^2(u)}. \quad (\text{E13})$$

which converges both in the UV and the IR.

Figure 25 presents the numerical evaluation of the dissipated energy in units of hv_0/l , where $v_0 = (1 + 4\alpha)v_F$ is the low-energy edge-magnetoplasmon velocity in this model. We observe that it saturates to 1 at large coupling. The finiteness of the dissipated energy validates a posteriori that the high-energy description of electronic decoherence is valid as long as the average energy of the incoming excitation is large compared to $\alpha hv_0/l$.

As a final check, one can rederive Eq. (E12) by considering the reduced density operator for the low-energy electron/hole pair excitations. When assuming that even after relaxation, the wave packet remains well separated from the Fermi sea, one can assume that $\langle \psi(t_-)\psi^\dagger(t_+) \rangle_F \simeq v_F^{-1} \delta(t_+ - t_-)$ in (33a) and therefore $\mathcal{G}_{\text{MV},1}^{(e)}(t|t')$ can be approximated by an expression which corresponds to the statistical mixture of states $|g(t)\rangle$ ponderated by $|\varphi_e(t)|^2$. This naturally comes from the physical image of the incident electron emerging from the interaction in a quantum superposition of the coherent electron/hole pair clouds $|g(t)\rangle$ attached to the electron being at position $v_F t$. Two different positions $v_F t$ and $v_F t'$ of the electron being perfectly distinguishable, what comes out is the statistical mixture of coherent electron/home pair clouds for the low-energy edge-magnetoplasmon modes. Computing the average energy stored in this statistical mixture precisely leads to (E12) since all the states $|g(t)\rangle$ carry the same average energy.

APPENDIX F: LOW-ENERGY DECOHERENCE AND RELAXATION

At low frequency, the effective dipole associated with the interaction region does not respond to a dc bias and can thus be described in terms of a frequency dependent admittance $G(\omega)$ in series with a capacitor C_μ (see Fig. 7). As explained in Appendix C, the corresponding transmission

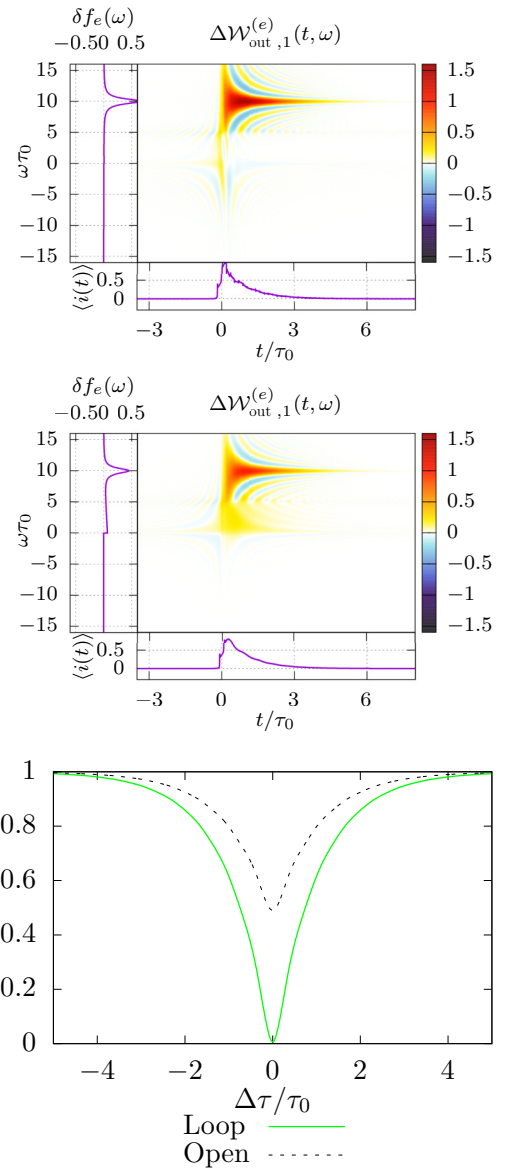


FIG. 26. Parameters are $w = 1 \mu\text{m}$, $d = 0.4 \mu\text{m}$, and $\omega_0 \tau_0 = 10$. The energy of the particle is $60 \mu\text{eV}$, the resonance energy is at $120 \mu\text{eV}$.

coefficient $t(\omega) = 1 - g(\omega)$ has modulus one if and only if $\Re(1/G(\omega)) = R_K/2$ meaning that the circuit involves the relaxation resistance $R_q = R_K/2$ in series with a purely reactive impedance. The simplest model for this pure reactance consists of an LC circuit depicted on the left panel of Fig. 7. The RC -time $\tau_0 = R_K C_\mu$ of the circuit corresponds to the time of flight of low-energy edge magnetoplasmons across the interaction region. Deviations from this behavior will lead to single-electron decoherence.

At low energy, since $t(\omega)$ is close to unity, perturbative expansion of $B_-(\omega)$ in convolution powers of $(1 - t(\omega))/\omega$ can be performed. Expanding also $t(\omega)$ in powers of $\omega \tau_0$ then leads to expressions of the low-energy elastic scattering amplitude in terms of the discrete element circuit parameters τ_0 , L , and C . The inelastic scattering probability across the

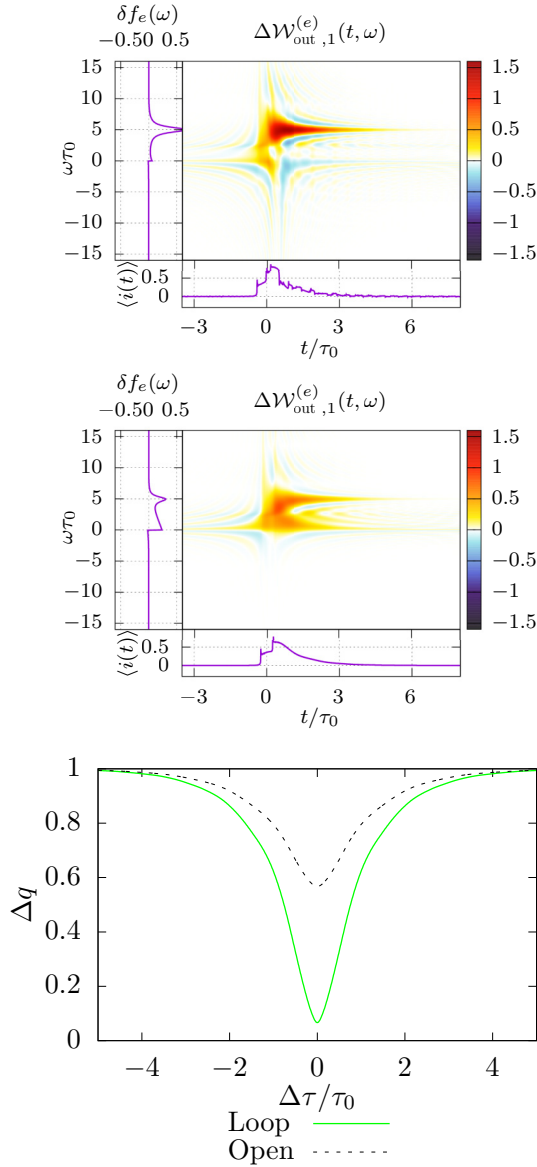


FIG. 27. Parameters are $w = 3 \mu\text{m}$, $d = 0.5 \mu\text{m}$, and $\omega_0\tau_0 = 5$. The energy of the particle is at $30 \mu\text{eV}$, the resonance energy at $45 \mu\text{eV}$. We see that sending a smaller energy excitation allows for larger loops.

interaction region is then given by

$$\sigma_{\text{in}}^{(\text{pert})}(\omega) = \frac{11\alpha_3^2}{180}(\omega\tau_0)^6 + \frac{5\alpha_3\alpha_5}{42}(\omega\tau_0)^8 + \mathcal{O}((\omega\tau_0)^9), \quad (\text{F1})$$

where the inductance L is directly related to the α_3 coefficient and the capacitance C only contributes to the next order:

$$\tau_0 = R_K C_\mu, \quad (\text{F2a})$$

$$\alpha_3 = \frac{L/R_K}{R_K C_\mu} - \frac{1}{12}, \quad (\text{F2b})$$

$$\alpha_5 = \frac{1}{80} - \frac{1}{4} \frac{L/R_K}{R_K C_\mu} + \left(\frac{L/R_K}{R_K C_\mu} \right)^2 \left(1 + \frac{C}{C_\mu} \right). \quad (\text{F2c})$$

This connects the inelastic scattering probability for an incoming electron to the low-frequency discrete element circuit description for the interaction region.

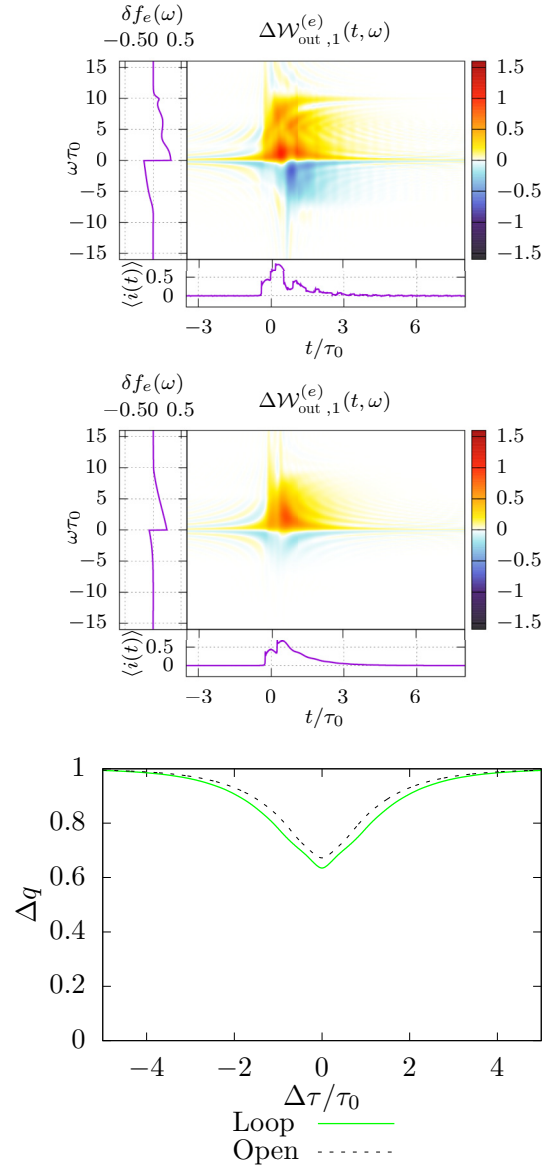


FIG. 28. Parameters are $w = 3 \mu\text{m}$, $d = 0.5 \mu\text{m}$, and $\omega_0\tau_0 = 10$. The energy of the particle is at $60 \mu\text{eV}$, the resonance energy at $45 \mu\text{eV}$. In that case, the loops does not allow protection from decoherence, and a plasmon state is emitted along with the electron.

A complementary understanding can be obtained by relating the finite-frequency admittance to the edge magnetoplasmon's effective velocity $v(\omega)$ within the interaction region using $t(\omega) = \exp(i\omega l/v(\omega)) = 1 - g(\omega)$. The effective circuit of Fig. 7 corresponds to a low-frequency expansion of $v(\omega)$ of the form

$$\frac{v(\omega)}{v_0} = 1 + \left(\frac{1}{12} - \frac{L/R_K}{R_K C_\mu} \right) (R_K C_\mu \omega)^2 \quad (\text{F3a})$$

$$- \left[\frac{C}{C_\mu} \left(\frac{L/R_K}{R_K C_\mu} \right)^2 - \frac{1}{12} \frac{L/R_K}{R_K C_\mu} + \frac{1}{180} \right] (R_K C_\mu \omega)^4 \quad (\text{F3b})$$

$$+ \mathcal{O}((\omega R_K C_\mu)^6), \quad (\text{F3c})$$

where $R_K C_\mu$ is the low-frequency time of flight l/v_0 . This expansion directly connects the discrete circuit element parameters L and C to the low-frequency behavior of $v(\omega)$. The value $L = C_\mu R_K^2/12$ corresponds to a frequency dependency $v(\omega) = v_0 + \mathcal{O}((R_K C_\mu \omega)^4)$. For $0 \leq L < C_\mu R_K^2/12$, the velocity of edge magnetoplasmons starts first to increase quadratically at low-frequency, whereas $v(\omega)$ directly starts decreasing for $L > C_\mu R_K^2/12$. Note that a higher inductance contributes to a stronger slow-down of the edge magnetoplasmons with increasing frequency, as expected for an inductive effect. The order 4 term given by Eq. (F3b) describes the behavior of the plasmon velocity beyond this first order and contributes to its decrease with increasing frequency.

Coming back to the electronic inelastic scattering probability given by Eq. (F1), the case where $L = R_K^2 C_\mu/12$ minimizes its growth: the first nonzero term is at order $(\omega\tau_0)^{10}$. This reflects the fact that for $L = R_K^2 C_\mu/12$, the distortion of a percussional current pulse is minimal at low-frequencies.

Finally, let us remark that the expansion of $\mathcal{Z}(\omega)$ up to order $(\omega\tau_0)^8$ only involves up to the second convolution power of $(1 - t(\omega))/\omega$, thus corresponding to the emission of at most two edge-magnetoplasmons. Processes with higher multiplasmon emission only contribute to higher powers in $\mathcal{Z}(\omega)$'s expansion. Keeping only the first convolution power

in the expansion would lead to

$$\sigma_{\text{in}}^{(1)}(\omega) = \frac{\alpha_3^2}{18}(\omega\tau_0)^6 - \frac{7\alpha_3\alpha_5}{60}(\omega\tau_0)^8 + \mathcal{O}((\omega\tau_0)^9), \quad (\text{F4})$$

which is the inelastic scattering probability arising from single edge-magnetoplasmon emission.

APPENDIX G: MORE EXPERIMENTALLY RELEVANT WIGNER FUNCTIONS

In this appendix, we show some more Wigner functions for loops built as in Fig. 24 of different sizes, and excitations of different energies (see Figs. 26–28). Velocities parameters are the same as in the main text, and Landau excitations have a typical time $\tau_0 = 100$ ps. All other parameters are shown below the corresponding Wigner functions. On all figures, the top panel shows a closed loop, whereas middle panel shows the case where both edge channels would stay outside of the loop and experience standard interaction along a length w . The bottom panel then displays the expected results of an HOM experiment for both cases. Using these figures, we can gain a more quantitative understanding of how changing the loop size or the injection energy impacts the experimentally accessible quantities.

-
- [1] C. Bauerle, D. C. Glattli, T. Meunier, F. Portier, P. Roche, P. Roulleau, S. Takada, and X. Waintal, *Rep. Prog. Phys.* **81**, 056503 (2018).
- [2] J. Splettstoesser and R. Haug, *Single-Electron control in Solid State Devices*, *Phys. Status Solidi B* **254** (2017) (the cover figure by the guest editors J. Splettstoesser and R. Haug).
- [3] E. Bocquillon, V. Freulon, F. Parmentier, J. M. Berroir, B. Plaçais, C. Wahl, J. Rech, T. Jonckheere, T. Martin, C. Grenier *et al.*, *Ann. Phys. (Berlin)* **526**, 1 (2014).
- [4] B. Roussel, C. Cabart, G. Fève, E. Thibierge, and P. Degiovanni, *Phys. Status Solidi B* **254**, 1600621 (2017).
- [5] A. Marguerite, E. Bocquillon, J.M. Berroir, B. Plaçais, A. Cavanna, Y. Jin, P. Degiovanni, and G. Fève, *Phys. Status Solidi B* **254**, 1600618 (2017).
- [6] A. Bertoni, P. Bordone, R. Brunetti, C. Jacoboni, and S. Reggiani, *Phys. Rev. Lett.* **84**, 5912 (2000).
- [7] R. Ionicioiu, G. Amaratunga, and F. Udrea, *Int. J. Mod. Phys. B* **15**, 125 (2001).
- [8] A. Bertoni, *J. Comput. Electron.* **6**, 67 (2007).
- [9] D. Pines and P. Nozières, *The Theory of Quantum Liquids* (Perseus Book, 1966).
- [10] L. Landau, *Sov. Phys. JETP* **5**, 101 (1957).
- [11] F. D. M. Haldane, *J. Phys. C: Solid State Phys.* **14**, 2585 (1981).
- [12] H. Steinberg, G. Barak, A. Yacobi, L. N. Pfeiffer, K. W. West, B. I. Halperin, and K. Le Hur, *Nat. Phys.* **4**, 116 (2008).
- [13] K. Le Hur, B. I. Halperin, A. Yacobi, *Ann. Phys.* **323**, 3037 (2008).
- [14] H. le Sueur, C. Altimiras, U. Gennser, A. Cavanna, D. Mailly, and F. Pierre, *Phys. Rev. Lett.* **105**, 056803 (2010).
- [15] A. Marguerite, C. Cabart, C. Wahl, B. Roussel, V. Freulon, D. Ferraro, C. Grenier, J. M. Berroir, N. Plaçais, T. Jonckheere *et al.*, *Phys. Rev. B* **94**, 115311 (2016).
- [16] V. Freulon, A. Marguerite, J. M. Berroir, B. Plaçais, A. Cavanna, Y. Jin, and G. Fève, *Nat. Commun.* **6**, 6854 (2015).
- [17] S. Tewari, P. Roulleau, C. Grenier, F. Portier, A. Cavanna, U. Gennser, D. Mailly, and P. Roche, *Phys. Rev. B* **93**, 035420 (2016).
- [18] I. P. Levkivskiy and E.V. Sukhorukov, *Phys. Rev. B* **78**, 045322 (2008).
- [19] A. O. Slobodeniuk, E. G. Idrisov, and E. V. Sukhorukov, *Phys. Rev. B* **93**, 035421 (2016).
- [20] G. Fève, A. Mahé, J. M. Berroir, T. Kontos, B. Plaçais, D. C. Glattli, A. Cavanna, B. Etienne, and Y. Jin, *Science* **316**, 1169 (2007).
- [21] F. Hohls, A. C. Welker, C. Leicht, L. Fricke, B. Kaestner, P. Mirovsky, A. Müller, K. Pierz, U. Siegner, and H. W. Schumacher, *Phys. Rev. Lett.* **109**, 056802 (2012).
- [22] J. Waldie, P. See, V. Kashcheyevs, J. P. Griffiths, I. Farrer, G. A. C. Jones, D. A. Ritchie, T. J. B. M. Janssen, and M. Kataoka, *Phys. Rev. B* **92**, 125305 (2015).
- [23] J. Dubois, T. Jullien, F. Portier, P. Roche, A. Cavanna, Y. Jin, W. Wegscheider, P. Roulleau, and D. C. Glattli, *Nature (London)* **502**, 659 (2013).
- [24] J. D. Fletcher, P. See, H. Howe, M. Pepper, S. P. Giblin, J. P. Griffiths, G. A. C. Jones, I. Farrer, D. A. Ritchie, T. J. B. M. Janssen *et al.*, *Phys. Rev. Lett.* **111**, 216807 (2013).
- [25] S. Hermelin, S. Takada, M. Yamamoto, S. Tarucha, A. Wieck, L. Saminadayar, C. Bärtle, and T. Meunier, *Nature (London)* **477**, 435 (2011).

- [26] J. Ott and M. Moskalets, [arXiv:1404.0185](https://arxiv.org/abs/1404.0185).
- [27] V. Kashcheyevs and P. Samuelsson, *Phys. Rev. B* **95**, 245424 (2017).
- [28] M. Misiorny, G. Fève, and J. Splettstoesser, *Phys. Rev. B* **97**, 075426 (2018).
- [29] A. Marguerite, B. Roussel, R. Bisognin, C. Cabart, M. Kumar, J. M. Berroir, E. Bocquillon, B. Plaçais, A. Cavanna, U. Gennser *et al.*, [arXiv:1710.11181](https://arxiv.org/abs/1710.11181).
- [30] B. Roussel, C. Cabart, R. Bisognin, G. Fève, and P. Degiovanni (unpublished).
- [31] N. Johnson, J. D. Fletcher, D. A. Humphreys, P. See, J. P. Griffiths, G. A. C. Jones, I. Farrer, D. A. Ritchie, M. Pepper, T. J. B. M. Janssen *et al.*, *Appl. Phys. Lett.* **110**, 102105 (2017).
- [32] P. Degiovanni, C. Grenier, and G. Fève, *Phys. Rev. B* **80**, 241307(R) (2009).
- [33] D. Ferraro, B. Roussel, C. Cabart, E. Thibierge, G. Fève, C. Grenier, and P. Degiovanni, *Phys. Rev. Lett.* **113**, 166403 (2014).
- [34] C. Altimiras, H. le Sueur, U. Gennser, A. Cavanna, D. Mailly, and F. Pierre, *Phys. Rev. Lett.* **105**, 226804 (2010).
- [35] P.-A. Huynh, F. Portier, H. le Sueur, G. Faini, U. Gennser, D. Mailly, F. Pierre, W. Wegscheider, and P. Roche, *Phys. Rev. Lett.* **108**, 256802 (2012).
- [36] R. Glauber, *Phys. Rev.* **130**, 2529 (1963).
- [37] C. Grenier, R. Hervé, E. Bocquillon, F. D. Parmentier, B. Plaçais, J. M. Berroir, G. Fève, and P. Degiovanni, *New J. Phys.* **13**, 093007 (2011).
- [38] G. Haack, M. Moskalets, J. Splettstoesser, and M. Büttiker, *Phys. Rev. B* **84**, 081303 (2011).
- [39] G. Haack, M. Moskalets, and M. Büttiker, *Phys. Rev. B* **87**, 201302 (2013).
- [40] D. Ferraro, A. Feller, A. Ghibaudo, E. Thibierge, E. Bocquillon, G. Fève, C. Grenier, and P. Degiovanni, *Phys. Rev. B* **88**, 205303 (2013).
- [41] A. Mahé, F. D. Parmentier, G. Fève, J. M. Berroir, T. Kontos, A. Cavanna, B. Etienne, Y. Jin, D. C. Glattli, and B. Plaçais, *J. Low Temp. Phys.* **153**, 339 (2008).
- [42] A. Mahé, F. D. Parmentier, E. Bocquillon, J. M. Berroir, D. C. Glattli, T. Kontos, B. Plaçais, G. Fève, A. Cavanna, and Y. Jin, *Phys. Rev. B* **82**, 201309 (2010).
- [43] L. Levitov, H. Lee, and G. Lesovik, *J. Math. Phys.* **37**, 4845 (1996).
- [44] J. Keeling, I. Klich, and L. S. Levitov, *Phys. Rev. Lett.* **97**, 116403 (2006).
- [45] C. Altimiras *et al.*, *Nat. Phys.* **6**, 34 (2010).
- [46] R. Hanbury Brown and R. Twiss, *Nature (London)* **178**, 1046 (1956).
- [47] G. Baym, *Acta Phys. Pol. B* **29**, 1839 (1998).
- [48] E. Altman, E. Demler, and M. D. Lukin, *Phys. Rev. A* **70**, 013603 (2004).
- [49] T. Jullien, P. Roulleau, B. Roche, A. Cavanna, Y. Jin, and D. C. Glattli, *Nature (London)* **514**, 603 (2014).
- [50] E. Bocquillon, F. D. Parmentier, C. Grenier, J.-M. Berroir, P. Degiovanni, D. C. Glattli, B. Plaçais, A. Cavanna, Y. Jin, and G. Fève, *Phys. Rev. Lett.* **108**, 196803 (2012).
- [51] M. H. Devoret, D. Esteve, H. Grabert, G.-L. Ingold, H. Pothier, and C. Urbina, *Phys. Rev. Lett.* **64**, 1824 (1990).
- [52] S. M. Girvin, L. I. Glazman, M. Jonson, D. R. Penn, and M. D. Stiles, *Phys. Rev. Lett.* **64**, 3183 (1990).
- [53] W. H. Zurek, S. Habib, and J. P. Paz, *Phys. Rev. Lett.* **70**, 1187 (1993).
- [54] L. Tomonaga, *Prog. Theor. Phys.* **5**, 544 (1950).
- [55] L. Luttinger, *J. Math. Phys.* **4**, 1154 (1963).
- [56] X. G. Wen, *Phys. Rev. B* **41**, 12838 (1990).
- [57] I. Safi and H. J. Schulz, *Phys. Rev. B* **52**, R17040 (1995).
- [58] I. Safi and H. Schulz, in *Quantum Transport in Semiconductor Submicron Structures*, edited by B. Kramer (Kluwer Academic, Dordrecht, 1995), p. 159.
- [59] I. Safi, *Eur. Phys. J. D* **12**, 451 (1999).
- [60] P. Degiovanni, C. Grenier, G. Fève, C. Altimiras, H. le Sueur, and F. Pierre, *Phys. Rev. B* **81**, 121302(R) (2010).
- [61] W. Cauer, *Archiv für Elektrotechnik* **17**, 355 (1926).
- [62] O. Brune, *J. Math. Phys.* **10**, 191 (1931).
- [63] D. B. Chklovskii, B. I. Shklovskii, and L. I. Glazman, *Phys. Rev. B* **46**, 4026 (1992).
- [64] I. L. Aleiner and L. I. Glazman, *Phys. Rev. Lett.* **72**, 2935 (1994).
- [65] K. A. Matveev and L. I. Glazman, *Physica B: Condens. Matter* **189**, 266 (1993).
- [66] G. Roussely *et al.*, *Nat. Commun.* **9**, 2811 (2018).
- [67] E. Bocquillon, V. Freulon, J. M. Berroir, P. Degiovanni, B. Plaçais, A. Cavanna, Y. Jin, and G. Fève, *Nat. Commun.* **4**, 1839 (2013).
- [68] C. Grenier, J. Dubois, T. Jullien, P. Roulleau, D. C. Glattli, and P. Degiovanni, *Phys. Rev. B* **88**, 085302 (2013).
- [69] I. Petković, F. I. B. Williams, and D. C. Glattli, *J. Phys. D: Appl. Phys.* **47**, 094010 (2014).
- [70] M. Hashisaka, N. Hiyama, T. Akiho, K. Muraki, and T. Fujisawa, *Nat. Phys.* **13**, 559 (2017).
- [71] H. Inoue, A. Grivnin, N. Ofek, I. Neder, M. Heiblum, V. Umansky, and D. Mahalu, *Phys. Rev. Lett.* **112**, 166801 (2014).
- [72] A. Prêtre, H. Thomas, and M. Büttiker, *Phys. Rev. B* **54**, 8130 (1996).
- [73] T. Christen and M. Büttiker, *Phys. Rev. B* **53**, 2064 (1996).
- [74] T. Giamarchi, *Quantum Physics in One Dimension* (Clarendon Press, Oxford, 2004).
- [75] M. Stone, *Bosonization* (World Scientific, 1994).
- [76] C. Grenier, R. Hervé, G. Fève, and P. Degiovanni, *Mod. Phys. Lett. B* **25**, 1053 (2011).
- [77] E. Bocquillon, V. Freulon, J. M. Berroir, P. Degiovanni, B. Plaçais, A. Cavanna, Y. Jin, and G. Fève, *Science* **339**, 1054 (2013).
- [78] S. Ol'khovskaya, J. Splettstoesser, M. Moskalets, and M. Büttiker, *Phys. Rev. Lett.* **101**, 166802 (2008).
- [79] V. Volkov and S. Mikhailov, *Sov. Phys. JETP* **67**, 1639 (1988).
- [80] N. Kumada, H. Kamata, and T. Fujisawa, *Phys. Rev. B* **84**, 045314 (2011).
- [81] N. Kumada, P. Roulleau, B. Roche, M. Hashisaka, H. Hibino, I. Petković, and D. C. Glattli, *Phys. Rev. Lett.* **113**, 266601 (2014).
- [82] D. S. Wei, T. van der Sar, J. D. Sanchez-Yamagishi, K. Watanabe, T. Taniguchi, P. Jarillo-Herrero, B. I. Halperin, and A. Yacoby, *Sci. Adv.* **3**, e1700600 (2017).
- [83] C. Wahl, J. Rech, T. Jonckheere, and T. Martin, *Phys. Rev. Lett.* **112**, 046802 (2014).
- [84] E. Berg, Y. Oreg, E.-A. Kim, and F. von Oppen, *Phys. Rev. Lett.* **102**, 236402 (2009).

- [85] H. Kamata, N. Kumada, M. Hashisaka, K. Muraki, and T. Fujisawa, *Nat. Nanotechnol.* **9**, 177 (2014).
- [86] V. I. Talyanskii, J. M. Shilton, M. Pepper, C. G. Smith, C. J. B. Ford, E. H. Linfield, D. A. Ritchie, and G. A. C. Jones, *Phys. Rev. B* **56**, 15180 (1997).
- [87] C. Leicht, P. Mirovsky, B. Kaestner, F. Hols, V. Kashcheyevs, E. Kurganova, U. Zeitler, T. Weimann, K. Pierz, and H. Schumacher, *Semicond. Sci. Technol.* **26**, 055010 (2011).
- [88] A. Imambekov, T. L. Schmidt, and L. I. Glazman, *Rev. Mod. Phys.* **84**, 1253 (2012).
- [89] I. Snyman and S. Florens, *New J. Phys.* **19**, 113031 (2017).
- [90] T. J. Suzuki, *Phys. Rev. B* **95**, 241302(R) (2017).
- [91] I. Snyman and S. Florens, *Phys. Rev. B* **92**, 085131 (2015).
- [92] M. Kanász-Nagy, Y. Ashida, T. Shi, C. P. Moca, T. N. Ikeda, S. Fölling, J. I. Cirac, G. Zaránd, and E. A. Demler, *Phys. Rev. B* **97**, 155156 (2018).
- [93] P. Dutta and P. M. Horn, *Rev. Mod. Phys.* **53**, 497 (1981).
- [94] A. Braggio, D. Ferraro, M. Carrega, N. Magnoli, and M. Sassetti, *New J. Phys.* **14**, 093032 (2012).
- [95] E. G. Dalla Torre, E. Demler, Th. Giamarchi, and E. Altman, *Nat. Phys.* **6**, 806 (2012); *Phys. Rev. B* **85**, 184302 (2012).
- [96] V. Freulon, PhD thesis, Ecole normale supérieure - ENS Paris, 2014.
- [97] H. Kamata, T. Ota, K. Muraki, and T. Fujisawa, *Phys. Rev. B* **81**, 085329 (2010).
- [98] I. Petković, F. I. B. Williams, K. Bennaceur, F. Portier, P. Roche, and D. C. Glatli, *Phys. Rev. Lett.* **110**, 016801 (2013).
- [99] R. Forster, *Bell Syst. Tech. J.* **3**, 259 (1924).
- [100] C. Neuenhahn and F. Marquardt, *New J. Phys.* **10**, 115018 (2008).
- [101] C. Neuenhahn and F. Marquardt, *Phys. Rev. Lett.* **102**, 046806 (2009).
- [102] G.-L. Ingold and Y. Nazarov, *Single Charge Tunneling*, NATO ASI Series B Vol. 294 (Plenum Press, New York, 1992), Chap. Charge tunneling rates in ultrasmall junctions, pp. 21–107.